Processing of Boron Carbide

A Thesis
Presented to
The Academic Faculty

by

Namtae Cho

In Partial Fulfillment
of the Requirements for the Degree
Doctor of Philosophy

School of Materials Science and Engineering
Georgia Institute of Technology
August 2006

Processing of Boron Carbide

Approved by:

Professor Robert Speyer, Adviser
School of Materials Science and Engineering
Georgia Institute of Technology

Professor Kenneth Sandhage
School of Materials Science and Engineering
Georgia Institute of Technology

Professor Robert L. Snyder
School of Materials Science and Engineering
Georgia Institute of Technology

Dr. James W. McCauley
Army Research Laboratory

Professor Thomas H. Sanders, Jr.
School of Materials Science and Engineering
Georgia Institute of Technology

Date Approved: June 22, 2006

ACKNOWLEDGEMENTS

I would like to express my deepest appreciation to my advisor, Professor Robert F. Speyer for his guidance, patience, and support throughout this work. During three years at Georgia Tech., he has always been a kind, prudent and respectable teacher and the best friend to me. I would also like to thanks my committee members, Professors Robert L. Snyder, Thomas H. Sanders, Jr., Kenneth Sandhage and Dr. James W. McCauley for their valuable suggestions and discussions. I can not but expressing my sincere thanks to Professor Keunho Auh and Kwangbo Shim, at Hanyang University in Korea, for his concerns on my career and research. I also would like to thank Runrun Duan and my Korean colleagues in MSE, who have given great help for three years.

I would like to express special thanks to my family. I would not finish my work without help and prayer from my parents and sister. My family in Korea always showed me great concerns on my life in the USA. My parents have supported and encouraged me all the time. They have been the greatest father and mother to me. Especially, I really tanks for my father's technical support for classic ceramic processing.

Thanks, God!

TABLE OF CONTENTS

LIST OF TABLES

LIST OF FIGURES

SUMMARY

The processing of boron carbide powder including sintering optimization, green body optimization and sintering behavior of nano-sized boron carbide was investigated for the development of complex shaped body armor.

Pressureless sintered B_4C relative densities as high as 96.7% were obtained by optimizing the soak temperature, and holding at that temperature for the minimum time required to reach terminal density. Although the relative densities of pressureless sintered specimens were lower than that of commercially produced hot-pressed B_4C, their (Vickers) hardness values were comparable. For 4.45 cm dia. 1.35 cm height disk-shaped specimens, pressureless sintered to at least 93.0% relative density, post-hot isostatic pressing resulted in vast increases in relative densities (e.g. 100.0%) and hardness values significantly greater than that of commercially produced hot-pressed B_4C.

The densification behavior of 20-40nm graphite-coated B_4C nano-particles was studied using dilatometry, x-ray diffraction and electron microscopy. The higher than expected sintering onset from a nano-scale powder ($\sim$1500°C) was caused by remnant B_2O_3 not removed by methanol washing, keeping particles separated until volatilization, and the carbon coatings, which imposed particle to particle contact of a substance more refractory than B_4C. Solid state sintering (1500-1850°C) was followed by an arrest in contraction attributed to formation of eutectic liquid droplets of size more than 10$\times$ the original nano-particles. These droplets, induced to form well below known B_4C-graphite eutectic temperatures by the high surface energy of nanoparticles, are interpreted to have quickly solidified to form a vast number of voids in particle packing, which in turn, impeded continued solid state sintering. Starting at 2200°C, a permanent liquid phase formed which facilitated a rapid measured contraction by liquid phase sintering and/or compact slumping.

CHAPTER I

INTRODUCTION

Boron carbide is the third hardest material (Knoop: 2800, 100 g load [1]) next to diamond and cubic boron nitride. Combined with its low weight (theoretical density: 2.52 g/cm^3), it is the premier material for personal armor. It is used as a nozzle material for slurry pumping and grit blasting because of its excellent abrasion resistance, and for nuclear shielding applications based on boron's high neutron absorption cross section [2]. Its crystal structure is complex because of the highly covalent nature of its interatomic cohesion; twelve atom boron-rich icosahedra reside at the corners of a rhombohedron, and each icosahedron is bonded to six others via direct bonds, and three-atom inter-icosahedral chains reside between the icosahedra [3]. Limited substitution of boron for carbon in the icosahedra and chains allows boron carbide to exist as a solid solution from stoichiometric B_4C at 20 mol% carbon to 8.8 mol% carbon.

Mechanical as well as ballistic performance improves with decreasing porosity, i.e. with increasing fired relative density; however until recently, pressureless sintering of pure B_4C to high relative density has proven to be difficult. Achieving near-theoretical density had required hot pressing, which precludes the formation of complex shapes. Additives such as SiC, Al_2O_3, TiB_2, AlF_3 and W_2B_5 have been used as sintering aids to increase pressureless sintered density [4, 5, 6, 7], but the second phases formed often have deleterious effects on mechanical behavior [2]. The best known additive for B_4C is carbon, most successfully added in the form of phenolic resin, which distributes carbon around the B_4C particles, and also serves as a pressing agent. Relative densities up to 98% have been obtained using this additive [8].

In previous work [9, 10] in our laboratory using H. C. Stark HS grade (sintering grade, $d_{50} = 0.8$ μm) powder, the causes of limited densification were investigated, and methods for circumventing them were developed. The presence of B_2O_3 coatings on B_4C particles

delayed the onset of sintering until they volatilized away, and there were indications that the oxide coating facilitated B_4C particle coarsening. At temperatures starting at 2010°C, particle coarsening was attributed to the vapor evolved directly from B_4C particles. By extracting the B_2O_3 coatings via a H_2 or vacuum treatment at 1300°C, and heating rapidly from 2010°C to a soaking temperature of 2230°C, a relative density of 94.7% was achieved.

The use of nano-scale ceramic powder for sintering has the advantage of a highly active powder which will sinter at decreased temperatures [12, 13]. While avoiding rapid or abnormal grain growth during sintering can be difficult [14, 15], nano-grained theoretically dense microstructures have shown evidence of superplasticity [16, 17] which would facilitate net-shape fabrication of ceramic components. Further, ceramics obey a Hall-Petch relation; strength increases with the square root of decreasing grain size [18]. In the intermetallic TiAl, this trend was observed until the grain size decreased below 30 nm, after which the trend reversed [19]. Forming dense green bodies from nano-sized ceramic powders with minimal flaws can be challenging. For dry processing, extreme pressures are usually required to form a dense green body [20]. In wet processing, nano-sized powders can be difficult to disperse [21].

This thesis presents follow-up work with respect to optimizing the soaking temperature and time, issues with specimen size, and the merits of post-HIPing pressureless-sintered specimens. Methods to slip cast boron carbide armor and parts of complex shape, and further improvements and green body formation were investigated. The sintering reaction behaviors during heat-treatment of an early-stage version of nano-scale B_4C powder under development by PPG Industries, Inc., was evaluated. This work has elucidated interesting and unique behaviors of nano-powder during heat-treatment, and has laid the groundwork for development and processing of this powder toward the goal of formation of nano-grained boron carbide for armor and wear-resistant applications.

CHAPTER II

LITERATURE REVIEW

2.1 Boron Carbide

Boron carbide belongs to the important group of nonmetallic hard materials, which includes alumina, silicon carbide, and diamond [22]. Although it was first synthesized over a century ago, in 1883, by Joly , the formula B_4C was assigned only in 1934 [23] . Today a homogeneity range from $B_{4.3}C$ to $B_{10.4}C$ has been established. The composition of commercial boron carbide is usually close to a boron : carbon stoichiometry of 4 : 1, the stoichiometric limit on the high-carbon side. Boron carbide is an exceedingly hard material, inferior in hardness only to diamond and cubic boron nitride. In addition, it has a high melting point, high mechanical strength combined with low density, and high neutron cross section, and is a semiconductor [2].

2.1.1 Crystal Structure

Boron carbide can be considered as a prototype of the interstitial compounds of rhombohedral boron, which include $B_{12}C$, $B_{12}C_2Al$, $B_{12}S$, $B_{12}O_2$, $B_{12}As_2$, $B_{12}P_2$, and $B_{3-4}Si$. The crystal structure of these materials consists of icosahedra that occupy the corners of rhombohedron, and a chain of atoms that runs along the *c*-axis of the rhombohedron. For the most part, boron atoms occupy the points of the icosahedra. The second constituent C, Al, O in general occurs on the chain. The rigid framework of polyatomic units of closely bonded atoms is reflected in the refractory nature and great hardness [24].

Boron carbide is a solid solution with a reported homogeneity range of 8.8 to 20 mol% C, which correspond to $B_{10.4}C$ to B_4C respectively. Its outstanding hardness and low theoretical density have made it the preferred material for lightweight armor such as body armor or aircraft armor. It melts congruently at 2490°C (13.3 mol% C), and forms a eutectic with carbon at 2375-2400°C at a composition of 29 mol% C [2], which is shown in Figure 1.

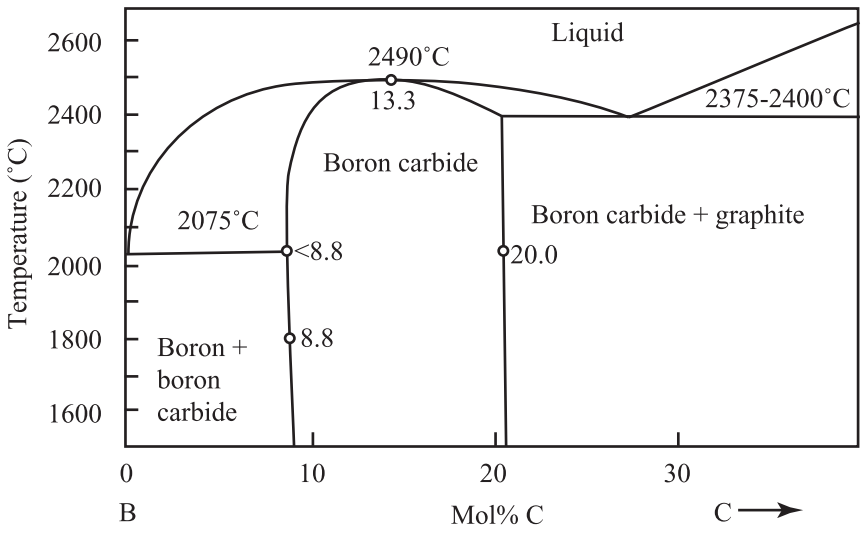

Figure 1: B-C phase diagram [2].

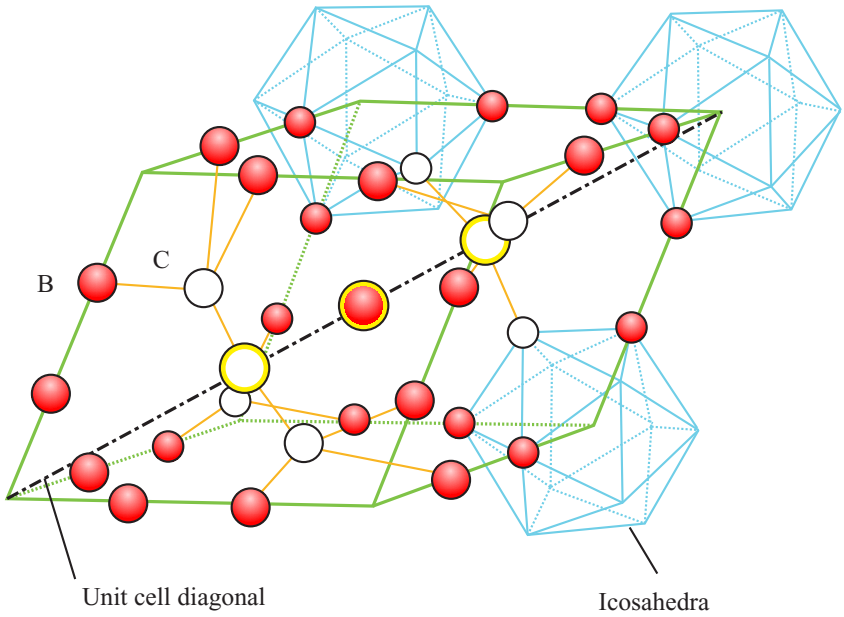

Figure 2: Rhombohedral unit cell structure of B_4C [2].

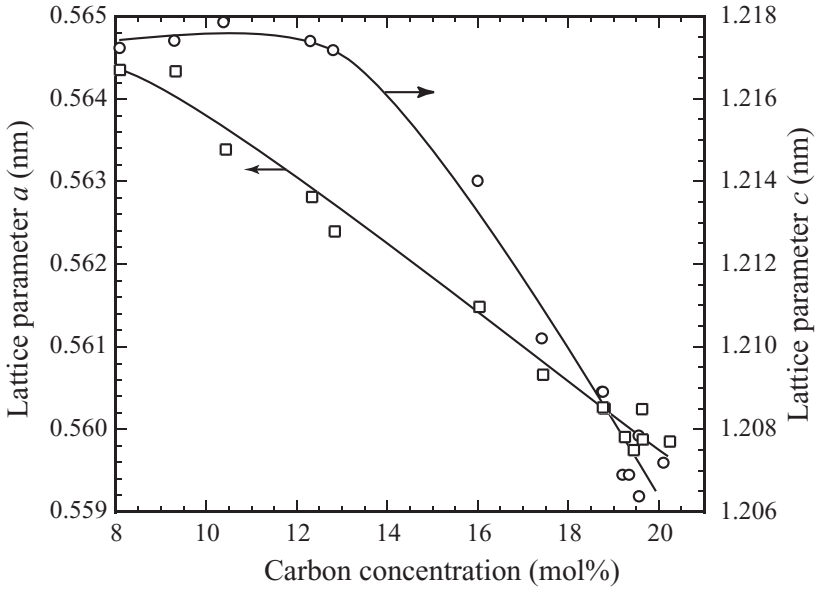

Figure 3: Lattice parameters of hexagonal B_4C unit cell based on the composition

B_4C solid solution adopts a rhombohedral unit cell structure consisting of 12-atom icosahedral units at the eight corners, which are joined by three-atom chains extending through the center of the unit cell as shown in Figure 2. As proposed by Emin [3], for stoichiometric B_4C, the icosahedra are $B_{11}C$ and the chains are C-B-C. As the boron content is initially increased, the carbons in the icosahedra are retained, while one of the carbons in each chain is replaced by boron. For compositions richer in boron than 13.3 mol% C ($B_{13}C_2$), some of the $B_{11}C$ icosahedra are then replaced by B_{12} icosahedra, while the chains remain C-B-B (as evidenced by a change in slope at this composition of the hexagonal c lattice parameter with boron additions [25] as shown in Figure 3 [26]). The volume of the unit cell decreases linearly with increasing carbon content. Correspondingly the theoretical density increases linearly with increasing carbon content, extending from 2.465 for $B_{10.4}C$ to 2.52 for B_4C.

More recent work by Kwei et al. [26] shows that in the C-B-C chain, the central boron atom is relatively loosely held and these locations can form vacancies. The formation of vacancies along the 3-atom chain with boron substitution decreases the thermal conductivity, as phonon transport increasingly resembles that thorough an amorphous material [27]. The increasing concentration of atomic defects has been attributed to weakly bound electrons,

which explains the increasing electrical conductivity with increasing boron content (with a break at 13.3 mol% C). Champagne and Angers found no significant change in elastic modulus or flexural strength over the solid solution range [28]. This conclusion was based on fitting to a model which simultaneously accounted for the effects of porosity, which were substantial, compared to those of composition (e.g. elastic modulus was reduced to 50% of the fully dense material by 13% porosity). Aslage et al. [2] found a significant drop in elastic modulus when the carbon concentration fell below the 13.3% C point, reflecting a change in stiffness of the most compressible structural unit, the icosahedra (i.e. when $B_{11}C \rightarrow B_{12}$).

2.1.2 Powder Manufacturing

Boron carbide is typically manufactured using boric acid and graphite; after thermal conversion of boric acid to boron oxide, boron carbide is formed via

$$2B_2O_{3(l)} + 7C_{(s)} \rightarrow B_4C_{(s)} + 6CO_{(g)}$$

where l, g, s stand for liquid, gaseous and solid phases. The process is strongly endothermic, 1812 kJ/mol or 9.1 kWh/kg, that is usually carried out at 1500 - 2500°C in an electric furnace. Either arc furnaces or resistance furnaces, analogous to Acheson furnaces for SiC, are used. The starting material is an intimate mixture of boric oxide and carbon, e.g., petroleum coke or graphite. Large quantities of carbon monoxide, 2.3 m^3/kg, are generated, and boron can be lost by evaporation of B_2O_3 at the high temperatures.

Since vapor pressure of boron oxide is relatively high at elevated temperature, vapor phase reaction should be considered. Given a partial pressure of carbon monoxide of one atmosphere, the above reaction has a negative standard Gibbs energy change about 1561°C. A temperature significantly higher than this is needed to promote reaction at a reasonable rate, unless the CO product is continuously removed from the furnace; generally more than 2000°C is required to synthesize boron carbide powder due to the very large amount of CO gas during the process as mentioned above.

Reactant boron oxide (B_2O_3) changes phase through the heating process. It melts at ∼452°C. Boron oxide yields a volatile suboxide (gas phase) B_2O_2 above ∼1227°C in

reducing environments. B_2O_2 boils at ~1860°C. The volatile B_2O_2 provides a gas-solid mechanism to synthesize boron carbide such as

$$C_{(s)} + B_2O_{3(l)} \rightarrow B_2O_{2(g)} + CO_{(g)}$$

$$5C_{(s)} + 2B_2O_{2(g)} \rightarrow B_4C + 4CO_{(g)}$$

The formation of boron carbide is highly dependent on the phase change of reactant boron oxide from solid to liquid to gaseous boron suboxide, such as $B_2O_{2(g)}$, and the effect of heating rate and ultimate temperature on the rate at which phase change occurs [29].

As an alternative fabrication method, boron carbide powders are also produced directly by magnesiothermic reductions of boric oxide in the presence of carbon at 1000 - 1800°C. MgO and unreacted Mg are removed by acid (H_2SO_4) washing [2].

$$2B_2O_{3(l)} + 6Mg_{(s)} + C_{(s)} \rightarrow B_4C_{(s)} + 6MgO_{(s)}$$

This reaction is strongly exothermic. It is carried out either directly by point ignition (thermite process) or in a carbon tube furnace under hydrogen. The product can be further purified by heating under vacuum at 1800°C. Since the MgO acts as a particle growth inhibitor, ultrafine boron carbide particles on the order of 0.1 - 1.5 μm are obtained.

2.1.3 Properties of Boron Carbide

The theoretical density of boron carbide increases linearly with carbon content within the homogeneity range of the solid solution. The relation ship can be described in following equation in the range of 8.8 at.% $\leq$ [C] $\leq$ 20.0 at%.

$$\rho(\mathrm{g/cm^3}) = 2.422 + 0.0048([\mathrm{C}]\ \mathrm{at.\%})$$

The density measured for stoichiometric B_4C is 2.52g/cm^3 [2]. Boron carbide is the third hardest materials known; however, the actual values of hardness are scattered, making comparisons difficult. Niihara et al. found the maximum hardness and indentation fracture toughness to be at the stoichiometric composition (Figure 4). The decrease in these values with increasing boron content, imply boron substitution contributes to a decrease in bond strength [30].

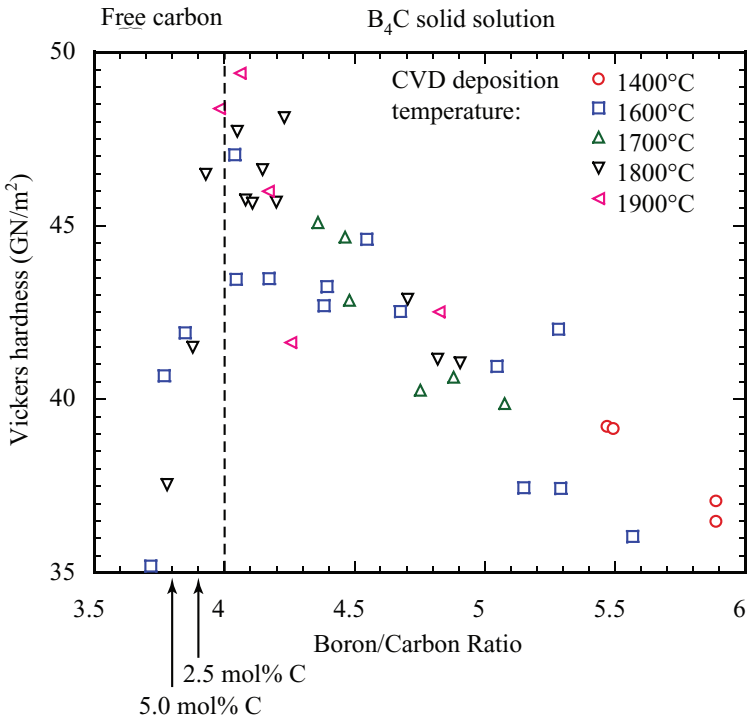

Figure 4: Hardness-depleting effects of increasing boron content in B_4C solid solution, or via increasing free carbon (graphite) in equilibrium with B_4C [30].

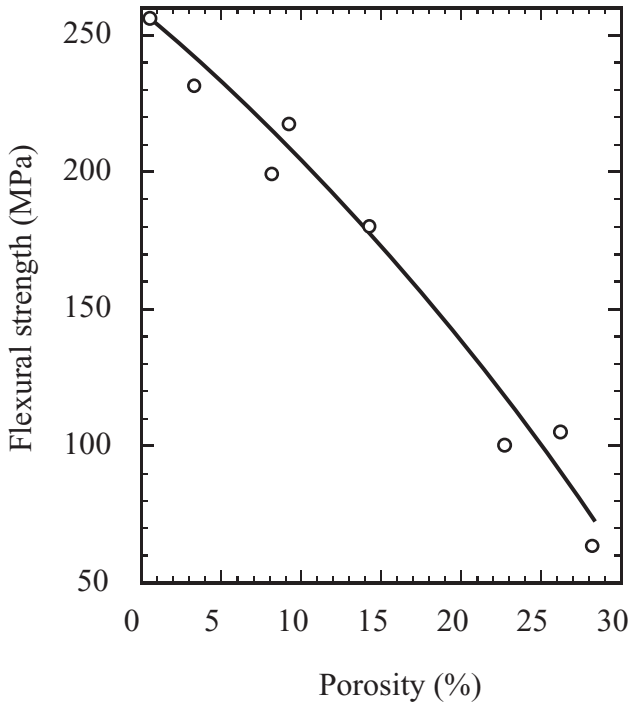

Figure 5: Flexural strength of boron carbide based on porosity [28].

Flexural strength increases with the carbon content within the homogeneity region. Beyond the homogeneity region, free graphite reduces strength. Thus, small amounts of boron are often added to eliminate free carbon in hot pressed boron carbide [28]. Flexural strength decreases with increasing porosity (as shown in Figure 5) and increasing grain size. The following relation was obtained by Knudsen using empirical data from hot pressed boron carbide [28, 31].

$$\sigma = \frac{\sigma_o}{D^a} \cdot exp(-bP)$$

$$ln\sigma = 20.337 - 0.362 lnD - 4.974\ P$$

where σ is the flexural strength, σ_o, a and b are constants, D is the mean grain size, and P is the volume fraction porosity. Values between 300 and 500 MPa were observed for strength.

Under a nitrogen atmosphere, there was little or no decrease in strength and fracture toughness of hot pressed boron carbide from its room temperature value of ∼350 MPa and ∼3.7 MPa·$m^{1/2}$ up to 1500 K, respectively. In air; however, there was a gradual decrease in strength between 600 and 1000°C due to oxidation to form B_2O_3/B_2O_2 and CO/CO_2. Si and Al addition s improved the oxidation resistance and resulted in the retention of higher strength at higher temperature. A relatively wide range of values of fracture toughness were measured by indentation and single edge notched bean methods (2.9 - 3.7 MPa·$m^{1/2}$). Fracture toughness is not greatly changed by beating up to 1200°C, even in air. Experimental values of Young's modulus (E) were scattered in the range of 360 - 460 GPa for fully sintered compacts.

$$E = 460 \left(\frac{1-P}{1+2.999P} \right) [GPa]$$

$$lnE = 26.833 - 5.462\ P[lnGPa]$$

$$E = 4.61 \times 10^{11} - 5.468 \times 10^7 T \times exp\left(\frac{-114.5}{T} \right)$$

A Poisson's ratio of 0.16-0.18 and shear modulus of 158-188 GPa for stoichiometric boron carbide were measured by different studies [32]. Table 1 shows the mechanical properties of various B_4C ceramics.

Table 1: Mechanical properties of various B_4C ceramics.

Property	Materials		
	B_4C Hot pressed	B_4C with 5% C	B_4C + TiB_2 (60:40)
Bulk density (g/cm^3)	2.51	2.51	3.30
Flexural strength (4point, 20°C, MPa)	480	560	730
Knoop hardness	2910	2860	2900
Fracture toughness (K_{IC}, MPa·m$^{1/2}$)	2.2	2.1	6.5
Young's modulus (GPa)	441	450	480
Mean grain size (μm)	5	2	5

2.1.4 Sintering of Boron Carbide

Sintering of pure boron carbide to high densities has historically proven difficult because of strong bonding and low plasticity in its solid form. Thus, hot pressing has been typically used to achieve near full density. B_4C powders are typically hot-pressed at ∼2100°C and 30-40 MPa to obtain dense articles [33, 34]. Angers and Beauvy hot pressed fine and pure B_4C at 2100-2200°C with 30-40 MPa for 15-45 min. They reported that three successive mechanisms during hot pressing result in the densification of B_4C: particle rearrangement, plastic flow leading to closing open porosity, and pore elimination at the end of the hot pressing by volume diffusion. Gogotsi and co-workers [35, 36] reported that hot pressed B_4C can be used as a structural materials in oxidizing atmospheres up to 600°C. In the temperature range of 600 - 1200°C, it showed tolerable oxidation resistance and satisfactory strength. Additives were used to lower the hot pressing temperature. Using 0.01 - 0.05 wt% of sodium silicate, magnesium nitrate and ferric oxide as additives, Vasilos and Dutta [34] hot pressed B_4C up to 98% of theoretical density at 1750°C under 0.167 MPa.

Hot pressing is only applicable to rather simple shapes. Therefore pressureless sintering of B_4C has been pursued in order to avoid expensive diamond machining for complex shapes. Kuzenkova *et al.* [37] sintered abrasive garde B_4C powder (3 m^2/g surface area) up to 95% of theoretical density at 2250°C. Various additives have been used to promote densification of B_4C without pressure, e.g. Al_2O_3, TiB_2, AlF_3 and W_2B_5 [5, 6, 7, 38]. Though those additives improved the densification of B_4C, they have facilitated exaggerated grain growth,

and diminished fracture strength [2].

The best known additive for pressureless sintering of B_4C is carbon. Carbon additions have usually been through in-situ pyrolysis of a phenolic resin which serves as a pressing agent, and yields ∼30 wt% carbon upon decomposition. Schwetz and Vogt [8] first used carbon additive in the form of phenolic resin for very fine, pure, stoichiometric B_4C with 10-22 m^2/g surface area. They observed that added carbon facilitated densification up to 98% of theoretical density at 2150°C. Concurrently, other independent studies also proved the importance of the carbon additive [39, 40]. Suzuki *et al.* [39] sintered B_4C with 25-30 wt% carbon additions up to 90-93% of theoretical density at 2250°C, and observed the formation of a liquid of the eutectic composition (30 %C). Later Schwetz and Grellner [41] studied the effect of carbon addition, microstructure and mechanical properties in detail. They found that only the use of B_4C starting powder with high surface area (above 15 m^2/g) and carbon addition could produce dense (greater than 95% of theoretical density) articles with a fine-grained microstructure. From the microstructure of pure B_4C in which both grain growth and pore growth with increasing temperature were observed, they concluded that shrinkage in pure B_4C is retarded due to a severe surface to surface transport mechanism (surface diffusion and vapor transport) and this surface to surface diffusion was inhibited by added carbon. Usually free carbon remains after firing of carbon-doped boron carbide. Using two organic precursors, it is possible to remove free carbon from sintered B_4C ceramics. Bougoin and Thevenot [42, 43] pressureless sintered B_4C with the addition of both carbon (phenolic resin) and silicon carbide (polycarbosilance) precursors. The resulting boron carbide had a relatively high density (of theoretical) and contained no free carbon and a small amount of SiC (∼5 wt%).

Post-sintering hot isostatic pressing (HIP) has been applied to carbon-doped B_4C in order to reach near-100% of theoretical density, which led to improvements in the flexural strength, modulus of elasticity, and wear resistance of the final product [41]. Free carbon has been shown to decrease hardness and indentation fracture toughness [30]. Free carbon is inevitably present in commercial sources of B_4C powder; small amounts of boron have been added to eliminate free carbon in hot pressed boron carbide [28].

The cause of limited densification in B_4C without additives has been established more clearly in recent years. Dole et al. observed highly coarsened sintered compacts of undoped B_4C after heat-treating at 2000°C, whereas carbon-doped samples had not yet undergone much coarsening [44, 45, 46]. It was suggested that B_2O_3 liquid in the starting B_4C powder may have provided a rapid diffusion path along particle surfaces, facilitating particle coarsening, and that C additions could eliminate B_2O_3 from boron carbide compacts.

Using a unique high-temperature differential dilatometer, Lee and Speyer [47] discerned particle coarsening processes that compete with sintering. Particle coarsening decreases the surface energy-based driving force for sintering, and results in lower achievable final densities.

The presence of B_2O_3 coatings on B_4C particles was implied via Figure 6; compacts heated to temperatures up to 1200°C initially lost weight, but then regained more than this weight over time after hydration of the oxide coatings by room air (forming, for example, orthoboric acid, H_3BO_3). After heating between 1200 and 1600°C, the vapor pressure of B_2O_3 became significant, whereby weight loss was substantial and permanent. Weight loss, which began again at temperatures exceeding 2010°C, corresponded to volatilization of B_4C, or its molecular subunits. Figure 7 shows the progression in densification, particle/grain size and weight loss for undoped specimens heated to specified temperatures, followed by furnace cooling. The vaporization of B_2O_3 coatings on the B_4C particles permitted direct B_4C-B_4C contact, and a surge in densification between 1870 and 2010°C. Weight loss and particle/grain coarsening, stalled between 1960 and 2010°C, and resumed thereafter. Coarsening and weight loss was then concurrent with slowed densification up to ∼2140°C. This corresponds to evaporation and condensation of B_4C, a coarsening mechanism typical of such covalently-bonded solids [48]. It is not established as to whether the evaporated gaseous species were molecular B_4C, or fragments of this molecule. Above 2140°C, densification accelerated significantly. Impurity-induced grain boundary liquid may have formed at and above this temperature. More likely, non-stoichiometric volatilization of B_4C left C behind (as indicated by X-ray diffraction results), accelerating sintering via enhanced grain boundary diffusivity of boron and carbon (activated sintering [48]), and inhibiting grain

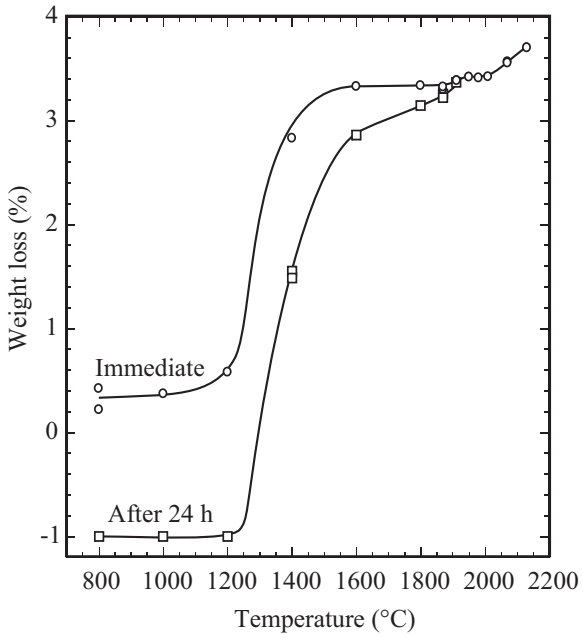

Figure 6: Weight changes in B_4C pressed pellets after heating to various quench temperatures at 50°C/min up to 1800°C, and 5°C/min above this temperature, under flowing He. Specimens were cooled in the furnace with the elements turned off under flowing He. Measurements were made immediately after removal from the furnace, and again after exposure to room air for one day [47].

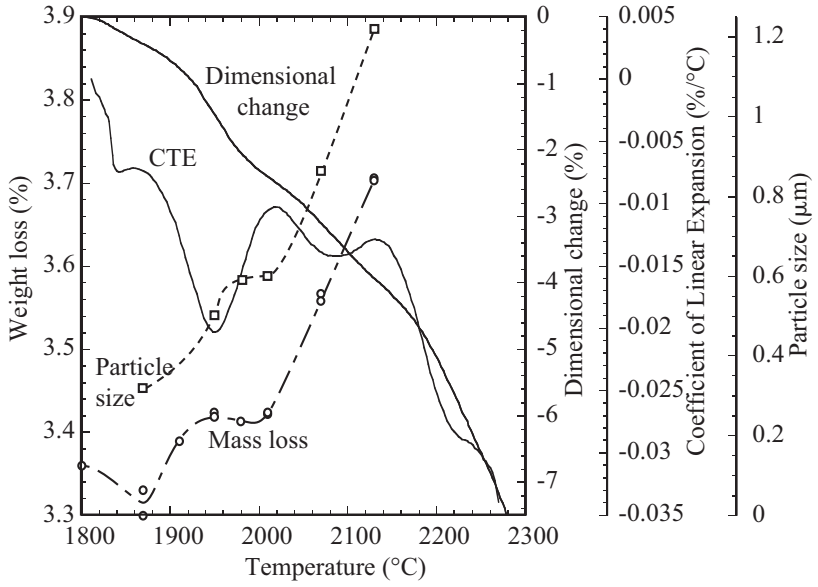

Figure 7: Trends in particle/grain size and weight change of samples after heating at 5°C/min up to specific maximum temperatures and then cooling with no soaking. Dilatometry-based dimension change and CTE (numerical temperature derivative) are also shown [47].

growth, keeping diffusion distances relatively short.

2.2 Ceramic Processing

2.2.1 Pressing

Dry powders or powders mixed with a small amount of binder solution are not a convenient feed material for dry pressing since they do not fill the die uniformly. Spray dried granules, which are soft agglomerates of particles, show better flow and die-filling characteristics. Spray dried granulated pressing powders typically contain deflocculant, binder (e.g. polyvinyl alcohol), plasticizer (e.g. polyethylene glycol) and lubricant (e.g. wax). The deflocculant is used to form a deflocculated suspension prior to spray drying. The plasticizer increases the deformability of the binder (separates polymer chains and promotes slippage between them). The binder hold the green ceramic part together for handling before firing. Soft wax and polyethylene glycol binders and plasticized polyvinyl alcohol also provide some lubricating action. The binder content is usually as low as practicable to minimize the vapor produced during binder burnout, and the associated green-body bloating defects possible during this process. A typical fill density for granulated powder is in the range of 25-35%. Vibration of particles in a pressing die can facilitate reorganization to more efficient packing, though this can be dependent on the vibration frequency and amplitude.

Dies and punches are usually made out of hardened steel, with clearance between die an punch designed to be smaller than the granule size. Uniaxial pressure is commonly in the range of 20-100 MPa, pressing pressures in excess of $\sim$100 MPa are said to be of diminishing utility and lead to accelerated die wear. Interparticle sliding during pressing is resisted by chemical adhesion and physical resistance produced by microscopic steps and asperities on particle surfaces. Lubrication is produced by an absorbed boundary layer of low friction or an interfacial fluid. Finely divided solids with a laminar molecular structure can also act as lubricants between abrasive particles, e.g. talc, graphite, and hexagonal boron nitride (often coined graphitic boron nitride). Superimposed vibrations may momentarily reduce the contact stress between some particles and aid in particle sliding. Particle compaction during uniaxial pressing of spray dried granules occurs in three

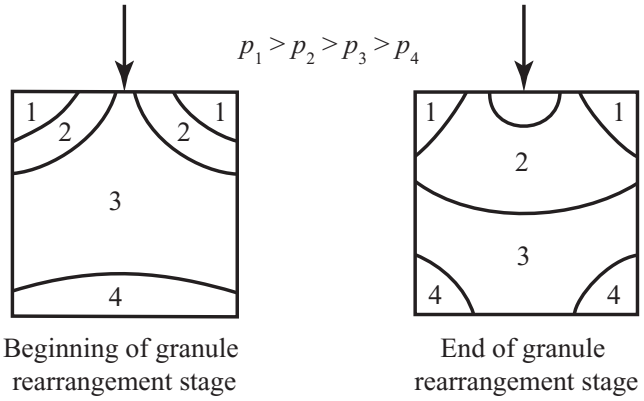

Figure 8: Pressure gradients within the powder in a die cavity when uniaxially pressed from above [49].

stages: granule flow and rearrangement, granule deformation and granule densification. Granules merge into a homogeneous mass during granule deformation, while during granule densification, particles within the granules slide and rearrange into slightly denser packing configurations. Pressures translated to compacting powders vary within the die because of die wall friction and particle translation radial to the pressing direction. The maximum pressure occurs near upper outer corners of the compact and diminishes toward the central axis. Pressing pressure decreases with increasing axial distance from the punch (Figure 8).

Non-uniform compaction can leave large pores; these defects are not eliminated by sintering and reduce the mechanical reliability of the part. Laminations and radial cracks are common defects occuring by differential elastic springback (caused by pressure gradients within the compact) when the punch is removed and the part is ejected. Such defects can be attenuated by decreasing the applied pressing pressure.

Uniaxial dry pressing is useful for pressing parts of relatively thin dimension in the pressing direction, in which differential green densities throughout the part are acceptably low. For parts of large volume or complex shapes, cold isostatic pressing (CIPing) is preferable. Parts are placed in rubber enclosures which are evacuated and sealed. These are in turn put in a water or oil bath which is pressurized typically to 200 MPa. This results in a green body of uniform green density with its complex shape retained.

2.2.2 Particle Size and Size Distribution

Smaller particle sizes facilitate increased sintering energy, and can result in fined-grained ceramics which have improved mechanical properties. Another important consideration, especially when scaling up to larger and more complex-shaped sintered parts, is green density. The higher the green density, either via dry pressing or casting from aqueous suspensions, the less extensive the shrinkage which occurs during firing, and the lower the propensity for warping and cracking defects.

Monosized spheres packed in cubic close packed or hexagonal close packed arrangements can theoretically achieve a green density of 74%; however, more realistic non-ordered arrangements of uniform spheres has been determined to be 60-64%. Higher green densities can be obtained when two sizes of spheres are used, one 1/7 the size of the other, in which the smaller spheres fill the interstitial spaces of the larger spheres. For continuous particle size distributions, it is considered better to have increasingly higher (number) concentrations in steps to smaller and smaller particle sizes (smaller particles have less volume, so more of them are required to fill the interstitial volumes). A log-normal distribution (i.e. after taking the logarithm of the distribution, the distribution appears Gaussian), typically followed by commercial powders, fulfills this requirement until very fine particle sizes are reached. For optimum green density, a log-normal distribution with as large a standard deviation as possible is desirable; green densities of $\sim$65% can be achieved. Particle size distributions which more strongly emphasize the relative proportions of fines, e.g. an Andreasen-type distribution, can result in further increases in green density to $\sim$77%. Broadening of the particle size distribution can be accomplished by blending of two or more different powder grades (i.e. powders of different average particle size).

Working against optimum green particle packing is the tendency of fine particles to form agglomerates (often through capillary forces from adsorbed surface moisture), or the presence of hard aggregates from the forming process of the powder. Non-spherical particles can form bridges, especially with rough particle surfaces, which are in turn frequently encountered in particles which have fractured through milling to form fine particle sizes. Lower green density is generally observed with higher aspect ratio (less round) particles.

2.2.3 Slip Casting

The surface chemistry of ceramic powders controls their charging behavior in aqueous suspension. Colloidal particles in deionized water tend to preferentially adsorb either OH^- or H_3O^+ ions to the particle surface, giving it a defined charge. Hydrated ions (ions surrounded by water molecules oriented to partially shield the ion charge) of opposite sign (counterions) surround the particle to compensate the surface charge. The hydrated ions in close proximity to the particle are tightly held via attractive forces to form a Stern layer. A higher concentration of counterions than in the bulk liquid are located in a diffuse layer (4-40 nm) extending away from the particle, completing the charge compensation.

Adding acids or bases to change the pH can effect the relative populations of adsorbed H_3O^+ and OH^-, changing the particle charge. For example, if the base NaOH were added, the concentration of H_3O^+ would decrease and the concentration of OH^- would increase in the liquid, and adsorbed on the particle surface as well (this assumes that the Na^+ ion is an indifferent ion, i.e. was not adsorbed by particles). For a particle with a net positive charge in deionized water, as the pH is increased by base additions (decreased H_3O^+ concentration), the net charge on the particle surface can be brought to zero (isoelectric point), and the surface charge then becomes increasingly negative with continued base additions.

When the surface charge is relatively high, the diffuse layer must extend out further to reach space charge neutrality. Particles with such extensive diffuse layers tend to repel, and a suspension of such particles will deflocculate. Additions of acid or base to a suspension of particles can be used to increase the surface charge, resulting in a wider diffuse layer, and deflocculate a suspension. This is mitigated at very high or low values of pH since the high concentration of electrolyte in solution narrows the width of the diffuse layers. Large monovalent cations (e.g. Rb^+ or NH_4^+) favor wide diffuse layers, while small divalent cations (e.g. Mg^{2+}) would do the opposite and tend to induce particles to coagulate. In the case of boron carbide, it is best to use acids or bases which do not introduce additional cations (e.g. Na^+) into the green cast (e.g. use nitric acid to decrease pH or ammonium hydroxide to increase it).

The tendency to deflocculate can be evaluated by viscosity measurements; interparticle

friction is attenuated in a well deflocculated suspension, hence measuring suspension viscosity as a function of pH will show minima in viscosity in pH regions of good deflocculation. The particle charge can be evaluated via the particle's motion in response to a potential difference. The location of the slippage plane for particle movement is near to but somewhat beyond the Stern layer. The potential at the slippage plane is called the zeta potential; if the zeta potential is high, then a broader diffuse layer is required to compensate the particle charge, and the tendency to deflocculate is greater. Regions in pH with maximum zeta potential are also regions of minimum viscosity.

An ionic polymer (polyelectrolyte, e.g. ammonium polyacrylate) in solution produces charged side groups and oppositely charged counter ions. The absorption of a polyelectrolyte may reverse the polarity of the particle surface and increase the charge on the particle. These can function as powerful deflocculants. Absorption of nonionic longer chain polymers can also function as a deflocculant by steric hindrance, in which the finger-like extensions of polymer chains from the particles keep the particles far enough away where van der Waals attraction does not draw them together.

Solids loadings typical for slip casting is in the 30-45% range. In a deflocculated suspensions, these loadings are beneficial in hindering preferential settling of the more coarse particles during casting.

Permeable molds for slip casting are commonly gypsum with 40-50% porosity and effective pore size of <5 μm. Slip casting under well controlled conditions can produce dense green bodies of complex shape. The gypsum mold slowly draws out the water of the suspension adjacent to the mold wall by the capillary forces of its open pores. As the water is extracted particles are deposited against the wall with moderately high packing efficiency. The cast thickness increases with the square root of casting time. A higher solids loading in the slurry increases the casting rate since there is less fluid to extract. Castings of higher green density require slower casting rates. Polymeric binder may be included in the suspension to give the body green strength, though typically < 1 vol% since it can contribute to coagulation. Separation of the piece from the mold normally occurs from the shrinkage of the cast on drying. Limitations of gypsum molds are their erosion in use due to their

low abrasion resistance and the significant solubility of gypsum in water. Improved porous polymer molds which combine higher porosity, relatively high mechanical strength and good elasticity have been developed for pressure casting applications. Elimination of the solvent produces the porous structure.

Williams and Hawn [50] found that by washing B_4C particles in methanol, the B_2O_3 coating converts to boric acid which in turn is converted to trimethyl borate which evaporates as an azeotrope with methanol. Powders striped of oxide showed better slip casting behavior. They prepared slip casting suspensions with 35 vol% solids loading. The isoelectric point was measured at a pH of 1, and the particles were negatively charged at all higher pH's (NH_4OH added as base). At pH > 6, the surface charge was sufficiently negative to deflocculate the suspension. Cast green densities as high as 65% were obtained.

2.3 Ceramic Armor

Ceramic armor is backed by a ductile organic composite such as graphite-reinforced plastic (e.g. polyethylene). The projectile is broken up by the hard ceramic surface, and the backing absorbs the energy of the projectile fragments and spreads the transmitted impulse. Armor designs which confine the ceramic armor plate are preferred, as they provide continued attenuation of the shock event. For conventional KE penetrators impacting confined ceramic targets, armor material responses and energy absorption mechanisms include brittle fracture/microcracking/comminution, spalling, punching (shearing, plugging), and radial fracture [22, 51, 52, 53]. Porosity in B_4C, as in all ceramics, decreases its fracture strength [28]. Upon impact from a projectile, microstructural inhomogeneities such as porosity and weak second phases can lead to local tensile fracture during passage of the initial shock wave, significantly lowering ballistic performance. Thus, ceramic armor must be sintered as closely as feasible to its theoretical density, particularly in the hypovelocity (velocity of the projectile is lower than the speed of sound through the armor material) ballistic impact regime.

CHAPTER III

EXPERIMENTAL PROCEDURE

3.1 Sintering Optimization

3.1.1 Sample Preparation

Commercially available B_4C powders (Grade HS, H. C. Starck, Berlin, Germany) were used in the as-received state. Table 2 shows the characteristics of the powder based on the manufacturer's data. Two powder stocks of Grade HS were used, one coded '00 (indicating year 2000), and the other coded '03 (2003). Powder compacts of B_4C with no additives were prepared by placing loose powder in die and punch assemblies of one of three sizes. Smaller specimens were uniaxially pressed under 250-300 MPa (Model No. 3925, Carver Inc., Wabash, IN) to form cylindrical pellets of 6.41 mm diameter and ∼5 mm in height, or 15.01 mm diameter and ∼3 mm in height. Larger disks of 44.45 mm diameter and ∼13.5 mm height were uniaxially pressed (Model V-50-1818-2TMX, Series 8323, Wasbash Metal Products Inc., Wabash IN) at increasing pressures of 100, 200, and 300 MPa, holding at each pressure for 5 min.

Table 2: B_4C powder characteristics

Surface area	18.8 m^2/g
Particle size	90% of particles $\preceq$ 2.99 μm
	50% of particles $\preceq$ 0.84 μm
	10% of particles $\preceq$ 0.24 μm
Impurity levels	1.50 wt% O
	0.41 wt% N
	0.022 wt% Fe
	0.055 wt% Si
	0.003 wt% Al
	0.23 wt% Other
Total boron	75.39 wt%
Total carbon	22.26 wt%
B/C molar ratio	3.76

Green compacts were also prepared using cold isostatic pressing (CIP). They were initially shaped using the steel dies and punches under 10 MPa of uniaxial pressure. CIPing of specimens encased in latex was then performed at either ∼200 MPa (Model CIP32260, Flow Autoclave Systems, Columbus, OH) or 413 MPa (Model CP360, American Isostatic Presses, Inc., Columbus, OH). For the latter pressure, increasing pressure to maximum occurred over ∼10 min, maximum pressure was then applied for ∼1 min, and pressure release followed over ∼2-3 min.

3.1.2 Sintering

The densification process of smaller samples was monitored by a differential dilatometer, as described previously [9, 10]. The infrared pyrometer used in the dilatometer was calibrated using the allotropic transformations of a pressed compact of high-purity iron (99.99+%, Sigma-Aldrich, St. Louis, MO), and the polymorphic transformations of high-purity ZrO_2 (99.99%, Aldrich, St. Louis, MO). The iron pellet was placed between alumina spacers, in turn in contact with the graphite pushrod and casing. Zirconia powder was uniaxially pressed into the shape of a cylindrical pellet and pre-sintered in a $MoSi_2$ box furnace in stagnant air at 1500°C for 5 h. This sintered pellet was then used as a calibration standard in the graphite dilatometer.

B_4C specimens were heated at 50°C/min to 1300°C and soaked in a flowing 50-50 vol% H_2-He mixture for 30 min, followed by soaking at that temperature for 2 h under flowing He. The specimens were then heated at 100°C/min to various temperatures in the range 2136-2336°C. They were then soaked at those temperatures until the contraction rate was less than 0.005%/min, after which time they were cooled to room temperature at 50°C/min (all of these specimens were '00). In a separate study, the same heat treatment schedule was used to reach 2298°C, and then specimens were soaked for various fixed time periods up to 150 min (all of these specimens were '03). For the 44.45 mm dia. specimens, the same furnace and similar temperature/atmosphere schedules were used with the dilatometer assembly removed.

After pressureless sintering, some specimens were hot isostatic pressed (i.e. post-HIPed,

American Isostatic Presses, Inc., Columbus, OH) by heating at 20°C to 2150°C, soaking for 125 min under 69-310 MPa of argon pressure, and cooling at 20°C/min.

3.1.3 Characterization

3.1.3.1 Density Measurements

Specimen densities were measured using Archimedes method. Percent relative densities were calculated based on a theoretical B_4C density of 2.52 g/cm^3. The dry weight (W_1) of each sample was measured just after sintering. The sample was then boiled in deionized water for more than 1 h and cooled to room temperature. The immersed weight in water (W_2) was measured in room temperature deionized water. Finally, the water-impregnated weight (W_3) was measured. Five measurements were made for each sample, and these values were averaged. The density ρ was calculated from:

$$\rho = \frac{W_1 \cdot \rho_W}{W_3 - W_2}$$

where ρ_W is the density of water (g/cm^3), which depends slightly on temperature.

$$\rho_W = 1.0017 - 0.0002315T$$

where T is equal to the water temperature in ^{o}C. The total porosity P (in percent) of the sample was calculated by following equation.

$$P = 100 \cdot \frac{\rho_{th} - \rho}{\rho_{th}}$$

where ρ_{th} is theoretical density of the sample.

3.1.3.2 Microstructural Characterization

Densified specimens mounted in plastic (Ultramount, Buehler, Lake Bluff, IL) were successively ground using 45, 15, and 9 μm diamond grinding discs (Metal-bonded diamond grinding discs, Buehler, Lake Bluff, IL and DP-Diamond Spray M, Struers, Westlake, OH) with water. The grind times and rotating speeds were ∼10 min and 150 rpm, respectively. Then specimens were then polished with 6, 3, and 1 μm diamond suspension (Metadi Supreme, Buehler, Lake Bluff, IL, and DP-Diamond Spray M, Struers, Westlake, OH) on

soft cloths (Texmet 1000, Buehler, Lake Bluff, Il). The polishing times and speeds were 30-60 min, and 200 rpm respectively. Specimens were rinsed with water after each step. The specimens were then removed from their plastic encasement.

Specimens ground and polished using the aforementioned procedure were then electrolytically etched for 1 min in a solution of 1% KOH, using 0.03 A/cm^2, applied using a current source meter (Model 2400, Keithley, Taunton, MA). The microstructure of etched specimens were characterized using scanning electron microscopy (SEM, Model S800, Hitachi, San Diego, CA, and Model 1530 SEM, LEO Electron Microscopy, Inc., Oberkochen, Germany). Average grain size and grain size distribution were determined using the linear intercept method, each based on 700 measurements on micrographs. SEM magnification was calibrated using a 300 mesh (84.67 μm line spacing) nickel calibration grid (Structure Probe, Inc., West Chester, PA).

3.1.3.3 Hardness Test

Indentation hardness of polished specimens was measured using a Vickers indenter (MHT series 200, Leco, St. Jospeh, MI) following the ASTM C1327-99 standard test method for advanced ceramics; specimens were indented with a 9.81 N load for 15 s at multiple locations until ten acceptable (as specified in the standard test method) indents were obtained. A commercially manufactured (uniaxially) hot-pressed B_4C specimen of dimensions 1 cm $\times$ 1 cm $\times$ 1.53 mm in thickness, was similarly polished and evaluated. Calibration of the indenter system was perforemd using WC-bast NIST standard reference material (SRM No. 2831). Based on five indentations, the measured hardness was 1599 $\pm$ 10 kg/mm^2, which was within 1.5% of the certified value of 1535 kg/mm^2.

3.1.3.4 Phase Identification

X-ray diffraction data (PW 1800 powder X-ray diffractometer, Philips, Mawah, NJ) was collected from 10 to 80° with scan speed of 1 s/setp and step size of 0.005°. Diffraction patterns of as-fired pellets were taken after the surface layer was ground away.

3.2 Green body optimization

3.2.1 Particle Size Analysis

To evaluate the potential for commercial powders other than Starck's, particle size distributions were evaluated using SEM. Powders were ultrasonically vibrated in ethanol for 20 min, and dried on polished aluminum SEM stubs. A 3×4 mosaic of high-resolution SEM micrographs was created (Adobe Photoshop). Using a digital drawing routine (Adobe Illustrator), each particle was drawn over. Particle agglomerates were then separated and the image was converted to a bitmap. Software was written (Visual Basic) which created arrays of pixels associated with each isolated particle. The diameter of a circle of equivalent pixel count was determined for each particle, and a cumulative percent finer plot was generated.

3.2.2 Oxidation Behavior of Boron Carbide

The tendency of boron carbide to oxidize at moderately low temperatures in air was evaluated by thermogravimetric analysis. Stark HS grade powder was soaked at various temperatures from 160 - 440°C with 40°C interval for 2 h. Also a 1 day soak was done at 300°C, and weight change behavior was monitored under a fixed heating rate (5°C/min).

3.2.3 Slip Casting

Slip-cast thimbles, pucks and quarter sized helmets were prepared from 15 vol% dispersions of B_4C in deionized water. The dispersions firstly made by mixing B_4C powder into deionized water and then, stirred and agitated with an ultrasonic probe (300W, 2 cm diameter tip) for 3 minutes. The pH, initially ∼3 for unwashed powder, was adjusted with 10% NH_4OH solution. The dispersions, which was aged for a day, was sonicated more times for 5 min and then stirred for ∼15 min with a three-blade propeller shaft mixer. The slip was deaerated in a vacuum desiccator and then poured into gypsum mold with a specific shape. After specific time based on the thickness and shape, green body was separated from the mold and dried in air for three days. The dried green bodies were pressureless sintered in He or vacuum atmosphere described in previous section.

3.3 Nano-particle Processing and Sintering

3.3.1 Sample Preparation

As-received nano-powders (PPG Industries, Inc, Pittsburgh, PA) were suspended in methanol and ultrasonicated (FS-14 Solid State Ultrasonicator, Fisher Laboratory Equipment Division, Pittsburgh, PA) for 1 min. The suspension was then placed in a warming oven at 80°C for 12 h to volatilize all fluid. The process was repeated three times for the purpose of removing boron oxide from the powder (∼50 wt%) [50]. Specimen powders of PPG#14 and #21 were exposed to repeated methanol washing in two different glass containers, a 100 ml beaker covered by aluminum foil with perforations, and a 10 ml vial also covered by perforated aluminum foil. The volume of methanol was determined based on weight measurements and an assumed density of 0.7917g/cm^3. Powder suspensions were agitated by placing the containers in an ultrasonicateing bath for 3 min. The containers were then placed in a warming oven at 65°C for ∼24 h, over which time all liquid was gently evaporated. Specimen weights were obtained immediately after removal from the warming oven, and again after exposure to room air for ∼24 h. The process was repeated multiple times.

Powder compacts were prepared by placing loose powder in a die and punch assembly under 150 MPa (Model No. 3925, Carver Inc., Wabash, IN) to form cylindrical pellets of 6.41 mm diameter and ∼5 mm in height.

3.3.2 Densification

The densification process was monitored by a differential dilatometer, as described previously. Specimens were heated under flowing helium (5.7 l/h) at 50°C/min to 800°C, and then 10°C/min to various quench temperatures, starting at 780°C in approximately 100°C increments up to 2298°C. Quenching consisted of furnace cooling with no power applied to the heating elements, and an increase in helium gas flow rate to 56.7 l/h. A full dilatometry trace was also recorded by heating a specimen at 50°C/min to 800°C, and then 10°C/min to 2300°C.

Specimens cooled in the dilatometer to room temperature after quenching were removed and immediately weighed. They were then exposed to room air for one day and weighed

again. Dimensional densities were determined for these quenched samples based on the two measured weights as well as volumes calculated based on caliper measurements of diameter and height. No measurable difference in specimen dimensions could be observed between those measured immediately after removal from the dilatometer and after 24 h exposure to room air.

3.3.3 Characterization

Specimens were prepared for transmission electron microscopy (TEM, JEOL 4000EX, Tokyo, Japan) by distributing particles on a lacey carbon TEM grid (Ted Pella, Inc., Redwood, CA). Images were taken of particles extending into the open-hole regions of the grid. Heat-treated powder compacts were fractured for observation in the scanning electron microscope (SEM, LEO 1530, Carl Zeiss MicroImaging, Inc., Thornwood, NY) in which no conductive coating was applied.

X-ray diffraction data (PANalytical X'Pert PRO X-ray diffractometer, Natick MA) was collected from 10 to 85°C with a scan speed of 1 s/step and a step size of 0.005°. Diffraction patterns were taken of the radial surfaces of as-fired pellets.

CHAPTER IV

RESULTS

4.1 Sintering Optimization

Figures 9 shows dilatometric traces in which specimens were heated at 50°C/min and then soaked at specific temperatures until the contraction rate was less than 0.005%/min. As the sintering temperature increased, the extent of contraction increased until 2298°C and decreased at 2317°C. The soaking period decreased with increasing soaking temperature. The dimension changes based on various soaking time at 2298°C is shown in Figure 10. Specimen expansion was detected as soaking time increased.

Figure 11 shows a selection of XRD traces. B_2O_3 was detected in the XRD pattern of the green compact. Based on the peak at 26.6° in 2θ, corresponding to the most intense peak of graphite, some free carbon was present in the as-received powder, and its relative proportion remained roughly constant after heat-treatments up to 2298°C. At soak temperatures of 2317°C and above, the greater intensity of this peak indicates an increase in graphite content. Peak splitting is apparent for the specimen heat-treated at 2336°C.

Figure 12 shows that during soaking at 2298°C, relative density and Vickers hardness both decreased, while the average grain size increased. After soaking for 17.5 min (time required to reach a shrinkage rate of 0.005%/min), no porosity was apparent within the grains (Figure 13a). Both polishing grain pull-outs as well as pores are depicted in the micrograph. As shown in Figure 13b, grain growth was far from uniform throughout the microstructure. After soaking for 150 min, pores are observed within grains and comparatively large fissures had formed at the grain boundaries (Figure 13c). Dilatometry traces (Figure 10) showed a gradual specimen expansion during the soaking period (e.g. the specimen soaked for 35 min showed a linear expansion of 0.38% over that time). XRD traces (not shown) as a function of soaking time showed seemingly random changes in relative intensities of B_4C peaks. No change in 2θ positions, the relative concentration of graphite, nor the formation

of any other phases, were detected.

Figure 14 shows the change in average grain size and grain size distribution with increasing soaking temperature. The soaking times at each of these temperatures were those required to reach a shrinkage rate of 0.005%/min (i.e. the termination of sintering), and these times decreased with increasing soaking temperature. Substantial grain growth was detected above 2298°C. A bimodal grain size distribution is apparent for the specimen soaked at 2317°C, whereas the grains appeared uniformly large after soaking at 2336°C, with substantial porosity embedded within the grains.

Figure 15 shows that the relative density increased with increasing soaking temperature up to ~2251°C, with maximum values over the range 2251-2298°C, and decreased after exposure to higher temperatures. The maximum relative density values (e.g. 96.7% for the specimen soaked at 2251°C) were markedly higher than those achieved in previous studies in our laboratory [9, 10]. Vickers hardness values followed the trends of relative density.

After post-HIPing a pressureless-sintered specimen, the relative density and hardness were significantly enhanced. The 44.45 mm diameter specimen ('03) shown in Figure 15 post-HIPed to full theoretical density and showed a remarkably high hardness. No changes in 2θ positions or relative intensities were observed as a result of post-HIPing. A typical microstructure of a post-HIPed specimen is shown in Figure 16.

The relative density of the commercial hot-pressed B_4C specimen was greater than the relative densities of pressureless sintered B_4C (Figure 15). The Vickers hardness values; however, were the same as the pressureless sintered specimens soaked in the range 2270-2298°C. Both the relative density and Vickers hardness of commercial hot-pressed B_4C were lower than those measured for pressureless sintered and post-HIPed B_4C. The intensity of the most intense XRD graphite peak was comparatively larger for the commercial hot-pressed B_4C specimen than for pressureless sintered or pressureless sintered followed by post-HIPed samples (compare the 2298°C and the commercial hot pressed B_4C XRD traces in Figure 11). A typical microstructure of the commercial hot-pressed B_4C specimen is shown in Figure 17; unique non-spherical pores, whose facets appear mutually oriented, appear within some grains, but not others.

Table 3: Pressing and heat-treatment parameters of samples of different sizes and their resulting relative densities.

No.	Lot year	Green body dia. (mm)	Uni-axial pres-sure (MPa)	CIP pres-sure (MPa)	Green relative density (%)	Sin-tering temp-erature (°C)	Soak time (min)	Fired relative density (%)	Post-HIP soak temp. (°C)	Post-HIP pres-sure (MPa)	Post-HIP relative density (%)
1.	'00	6.41	300	-	68	2251	60	96.2	2150	310	99.1
2.	'00	6.41	300	-	68	2251	45	96.7	2150	310	99.0
3.	'00	6.41	10	413	70	2251	45	96.2	2150	310	-
4.	'00	15.01	300	-	68	2251	60	96.0	2150	310	99.7
5.	'00	44.45	10	200	64	2251	60	93.0	2150	310	99.8
6.	'00	44.45	10	200	64	2222	60	92.4	2150	310	97.1
7.	'00	44.45	10	200	64	2222	60	93.2	2150	310	99.7
8.	'00	44.45	10	200	64	2222	60	93.1	2150	310	99.7
9.	'00	44.45	10	200	64	2222	60	91.3	2150	310	93.3
10.	'00	44.45	250	-	68	2222	45	95.7	2150	310	99.5
11.	'00	44.45	250	-	68	2222	60	95.3	2150	310	-
12.	'03	44.45	10	413	70	2251	40	95.3	2150	207	100.0
13.	'03	44.45	10	413	70	2251	40	95.3	2000	207	100.0
14.	'03	44.45	10	413	70	2251	40	95.2	2150	138	100.0
15.	'03	44.45	10	413	71	2251	40	95.3	2150	69	100.0

Table 3 enumerates pressing methods, resulting green, pressureless sintered, and post-fired HIPed relative densities, for specimens of differing sizes. The analytical balance used for Archimedes density measurements displayed a variation over time of ±0.01 mg. Based on propagation of random error, relative density errors of ± 0.14%, 0.04%, 0.00%, and 0.09% are expected for the 6.41 mm dia., 15.01 mm dia., 44.45 mm dia., and commercial hot-pressed samples, respectively. Small (6.41 mm dia.) samples either cold uniaxially or isostatically pressed to high green relative density (68-70%) displayed pressureless-sintered relative densities of 96.2-96.7% and post-HIPed to relative densities of 99.0-99.1%. Uniaxially pressed large (44.45 mm dia.) samples pressureless sintered to higher relative density (e.g. 95.3 and 95.7%) than those CIPed at 200 MPa; however, these samples showed radial cracking. The large (44.45 mm dia.) CIPed samples pressureless sintered to a slightly lower relative density than the small (6.41 mm dia.) CIPed or uniaxially-pressed samples. Near-theoretical relative densities (>99.5%) were obtained for the large samples which were CIPed and pressureless sintered, when their relative densities were 93.0% or higher prior to post-HIPing. CIPing large specimens at the higher pressure of 413 MPa resulted in higher green relative densities (70%). This combined with a higher sintering soak temperature and a shorter soaking time yielded pressureless sintered relative densities of 95.3%, which then post-HIPed completely to theoretical density (specimens 12-15 in the table). The same result was obtained with post-HIPing gas pressures as low as 69 MPa.

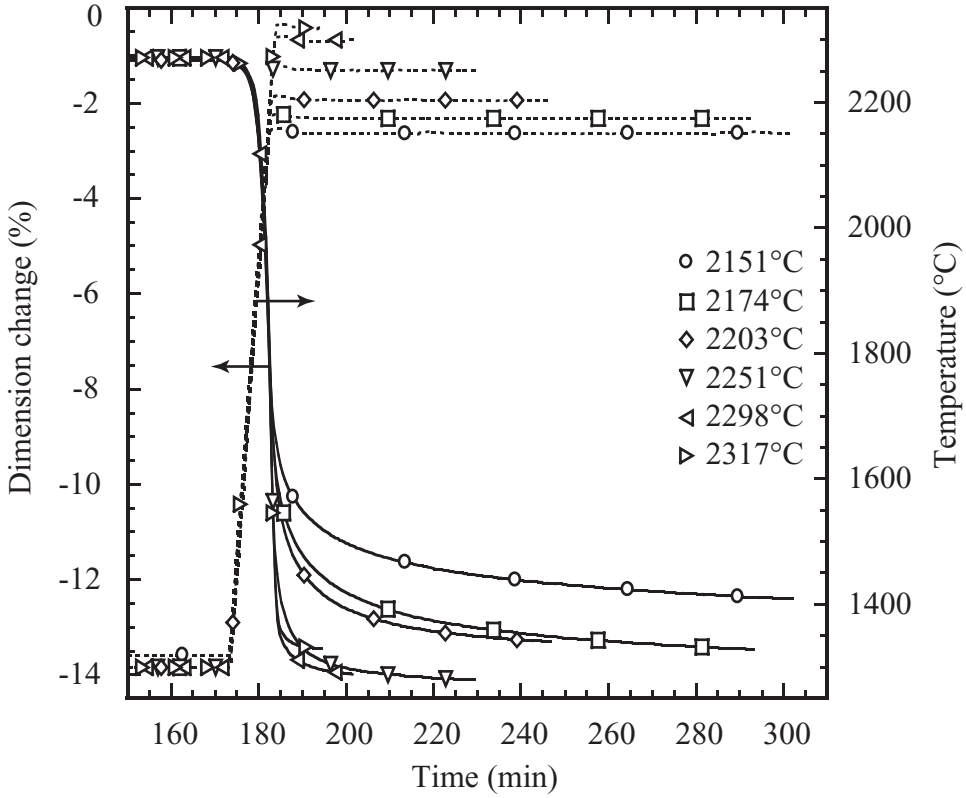

Figure 9: Dilatometry traces based on sintering temperature.

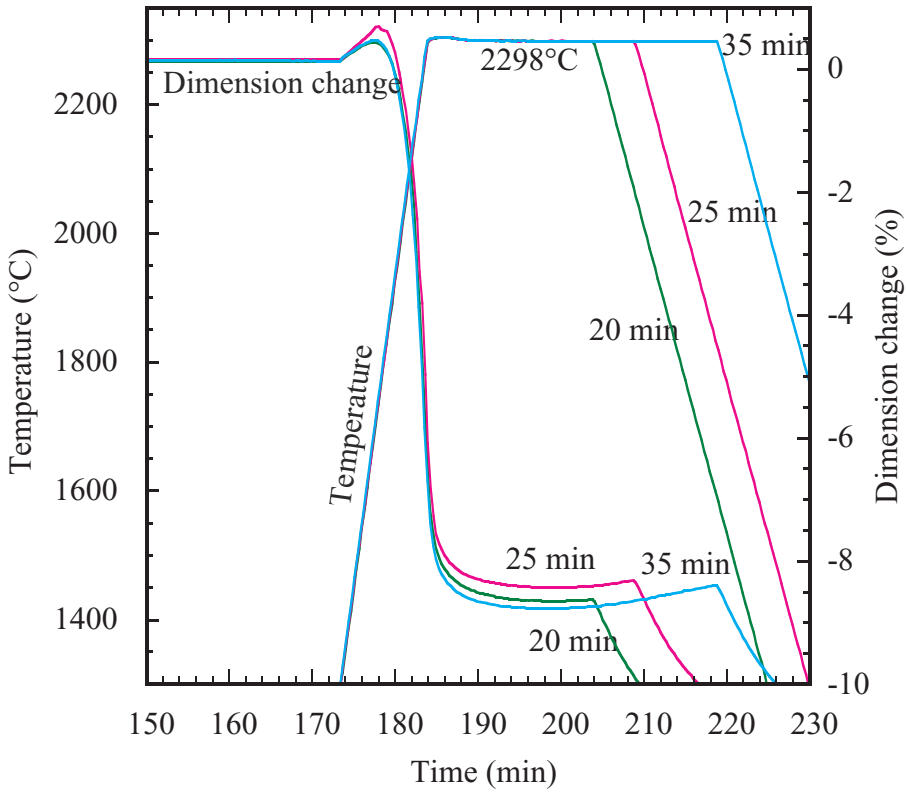

Figure 10: Dilatometry traces based on various sintering times at 2298°C.

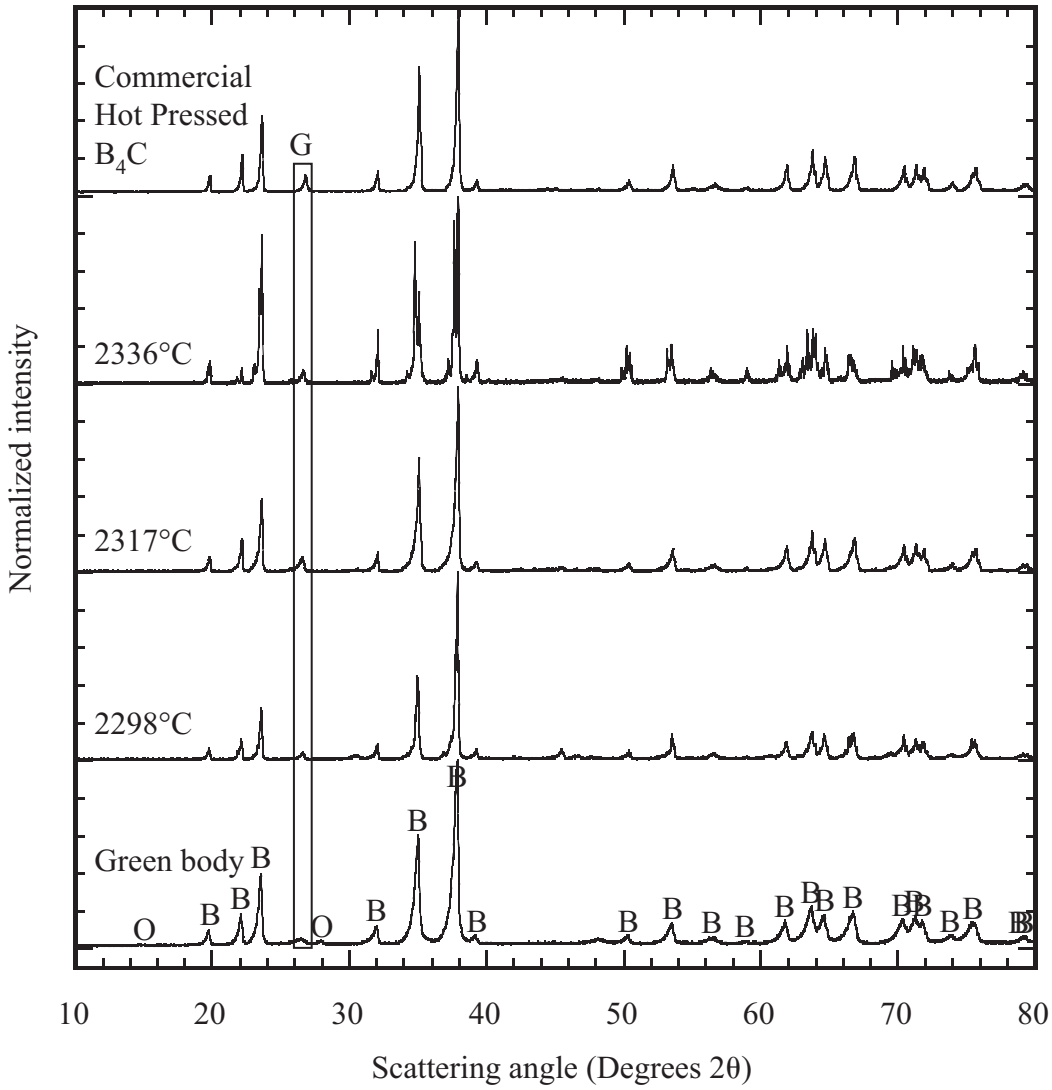

Figure 11: XRD traces of a selection of specimens heat-treated at various soak temperatures until their shrinkage rates were less than 0.005%, along with XRD patterns of as-received powder and a commercial hot-pressed B_4C specimen. Diffraction pattern intensities were normalized so that the intensities of the most intense peaks in each pattern were made equal. B: B_4C solid solution (ICDD: 37-0798), O: B_2O_3 (ICDD: 13-0570), G: carbon (graphite, ICDD: 75-2078).

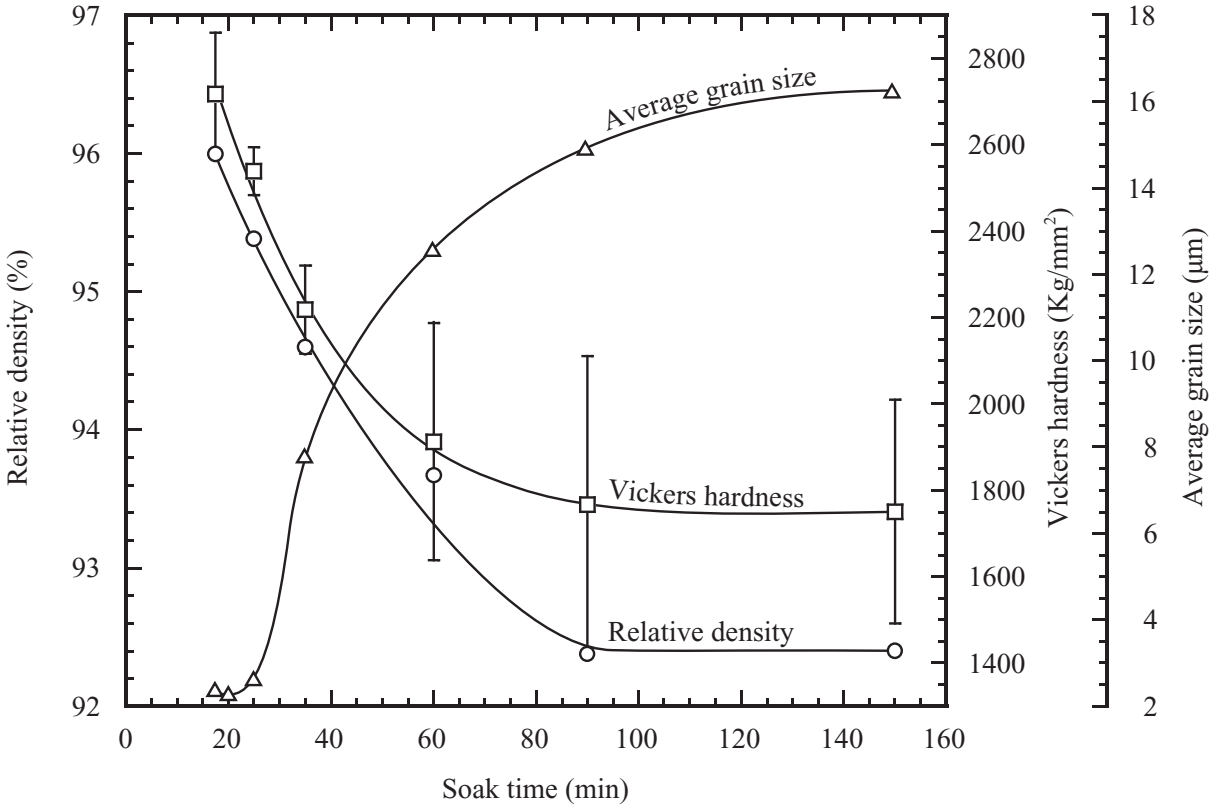

Figure 12: Decrease in Vickers hardness and relative density concurrent with an increase in average grain size, with increasing soaking time at 2298°C. Error bars represent standard deviations calculated from ten acceptable hardness measurements.

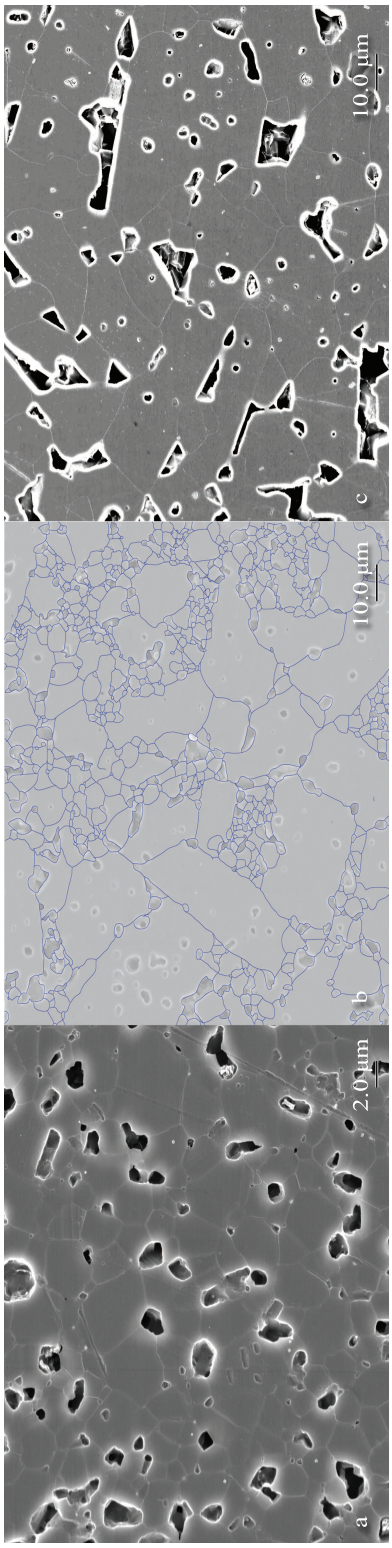

Figure 13: Specimens soaked at 2298°C for a) 17.5 min, b) 35 min (grain boundaries were drawn-over to facilitate visual clarity), and c) 150 min.

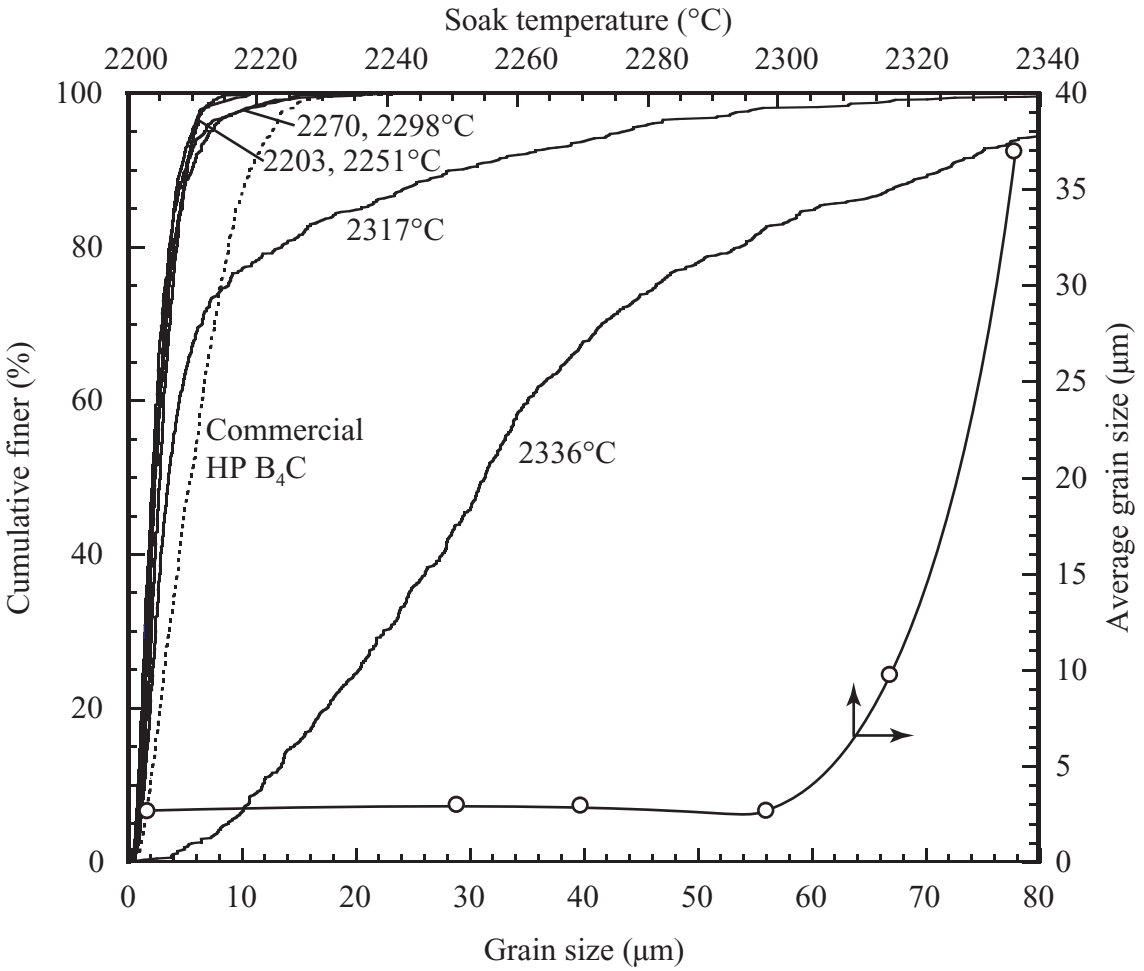

Figure 14: Average grain size as a function of soaking temperature (soaked until the shrinkage rate fell below 0.005%/min). Also shown are the grain size distributions for the various soaking temperatures along with the grain size distribution of the commercial hot-pressed B_4C specimen.

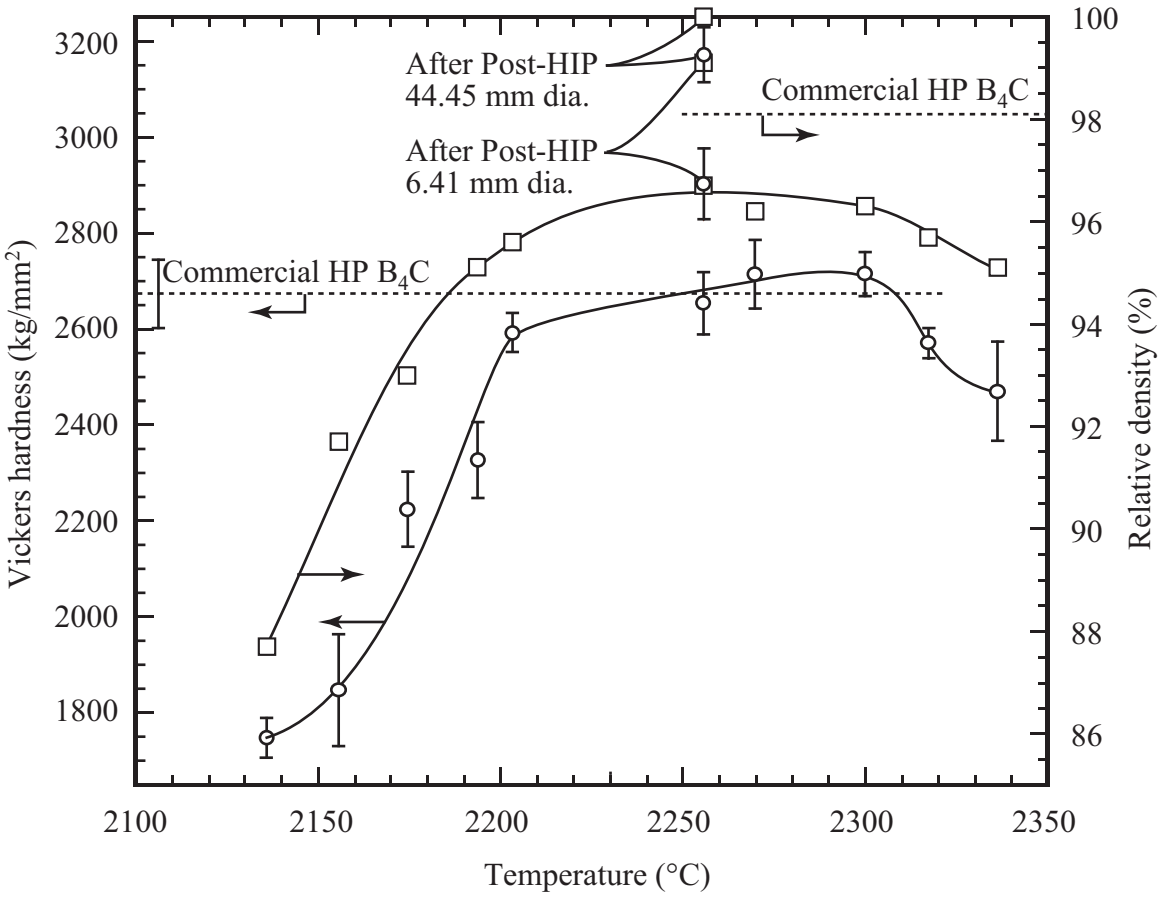

Figure 15: Relative densities and Vickers hardnesses measured for 6.41 mm dia. specimens after pressureless sintering at various soaking temperatures until the shrinkage rate was less than 0.005%/min. Error bars represent standard deviations calculated from ten acceptable hardness measurements. The relative density and Vickers hardness for post-HIPed samples of two different sizes are also shown, along with these values for a commercial hot-pressed B_4C specimen.

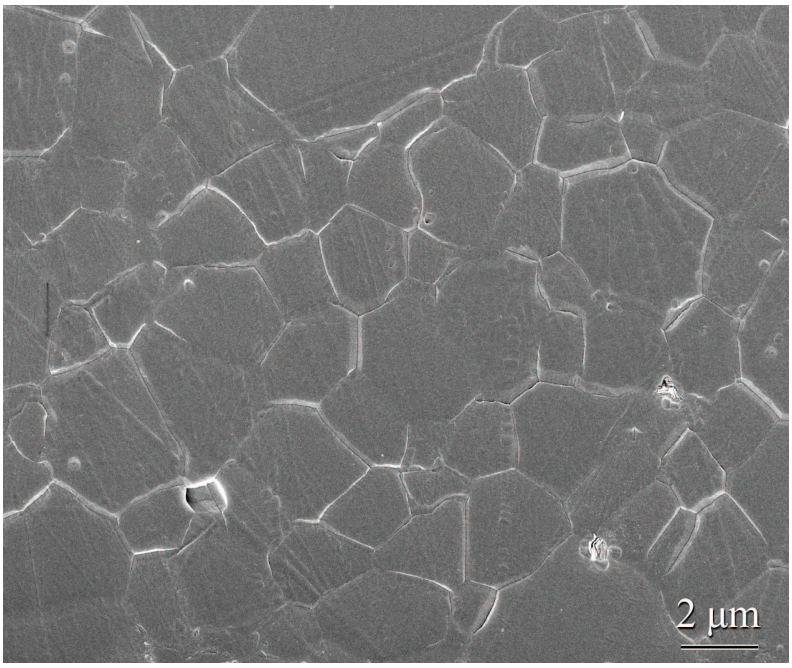

Figure 16: 6.41 mm diameter specimen pressureless sintered and post-HIPed at 2150°C and 310 MPa to 99.1% relative density.

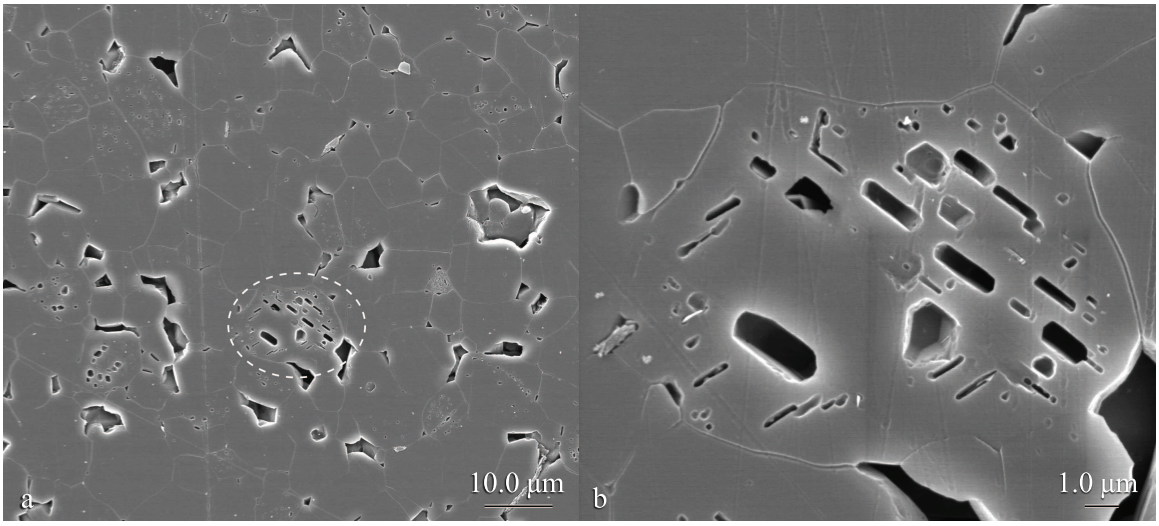

Figure 17: a) Commercially hot pressed B_4C specimen. b) Magnified view of circled region in a).

4.2 Green Body Optimization

4.2.1 Oxidation Behavior of Boron Carbide

Figure 18 show thermogravimetry results from loose powders specimens soaked in static air at various temperatures for 2 h (Figure 18 a), a 1 day soak at 300°C (Figure 18 b), and weight change behavior under a fixed heating rate (Figure 18 c). After initial removal of adsorbed water during heating, continued weight loss was observed during the 2 h soak for soak temperatures up to 320°C. Over 360°C, weight gain was observed. The cause of the weight loss has yet to be established, and is being investigated via XRD traces of specimen powders exposed to these thermal schedules.

During one day soaking as shown in Figure 18, the slope of weight loss was changed around 8 h. Under a constant heating rate, a slight weigh loss was observed over 160°C and a rapid weight gain was monitored over 400°C.

4.2.2 Particle Size Analysis

Figure 19 shows image converted from a mosaic of micrographs to create arrays of pixels associated with each isolated particle (confirmed by assigning each particle a different color using a random number generator). The diameter of a circle of equivalent pixel count was determined for each particle, and a cumulative percent finer plot (Figure 20) was generated. Based on generated plot (Figure 20), the median particle size (number percent) of stark HS‘00, d_{50}, was ∼0.1 μm. The stark HS‘00 powder shows the smallest d_{50} values with the broadest distribution. Based on converted data from the manufacturer as shown in Figure 21, and converted to cumulative percent as shown in Figure 22, the d_{50} was ∼0.2 μm. Thus far, the Starck powder sinters to significantly higher relative density than the powders from other companies.

4.2.3 Slip Casting

Slip casting suspensions were prepared in accordance with the results of Williams and Hawn [50]. A substantial difference in cast quality resulted from methanol washing and raising the pH of a ∼30% solids suspension (using ammonia) to 7.

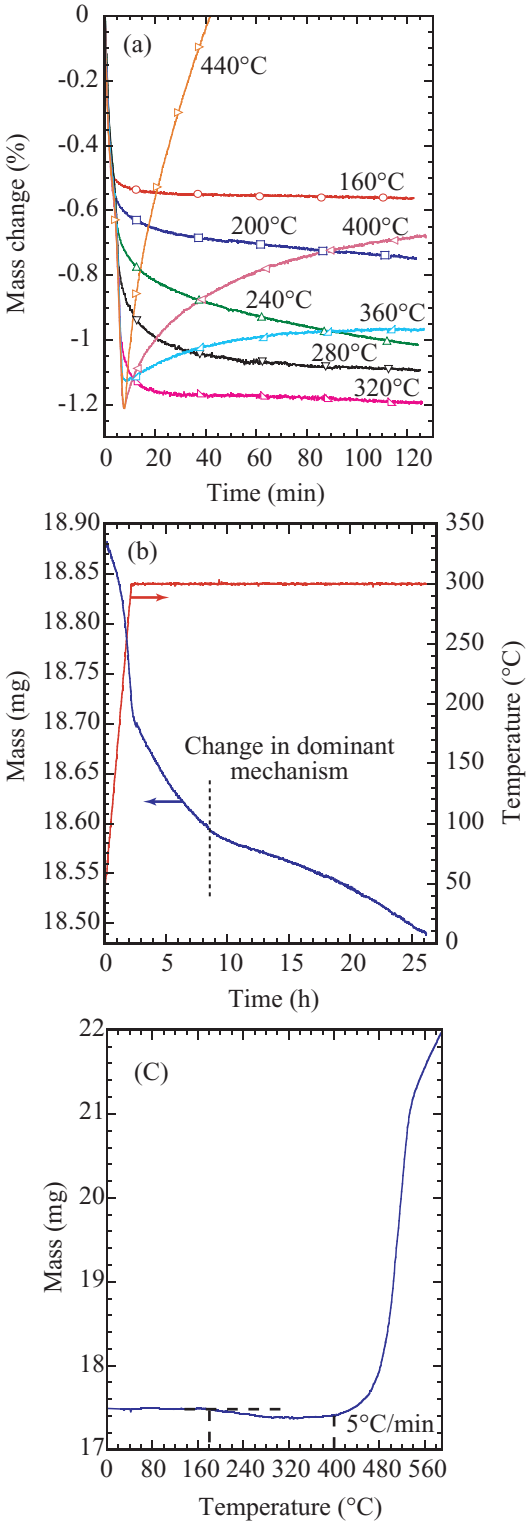

Figure 18: Thermogravimetric traces of B_4C powder (a) heat treated in static air at various temperature, (b) 1 day soaking at 300°C and (c) weight change at fixed heating rate.

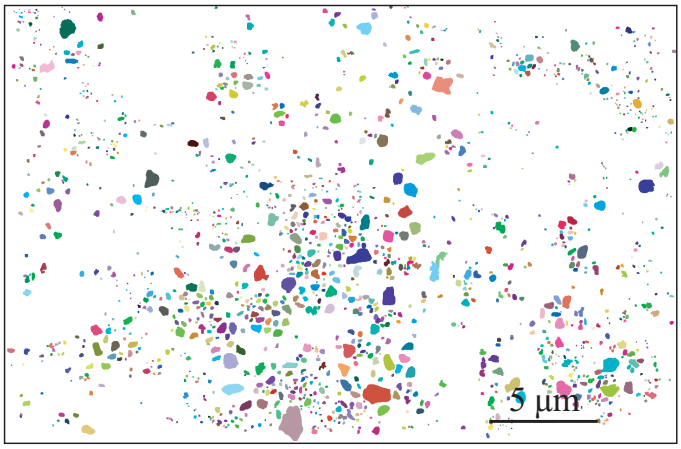

Figure 19: Image output from Visual Basic program which painted each particle a different color to show that each particle was uniquely recognized.

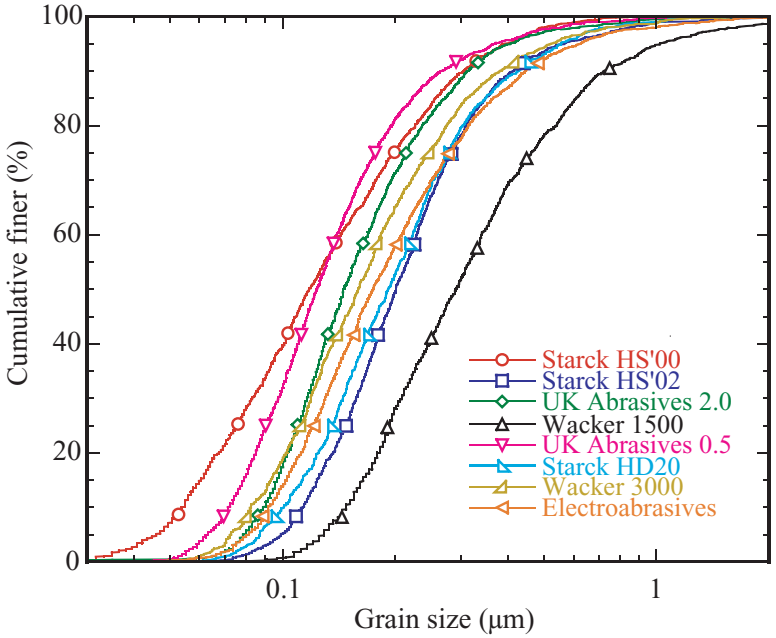

Figure 20: Cumulative percent finer plot for various commercial powders analyzed using SEM.

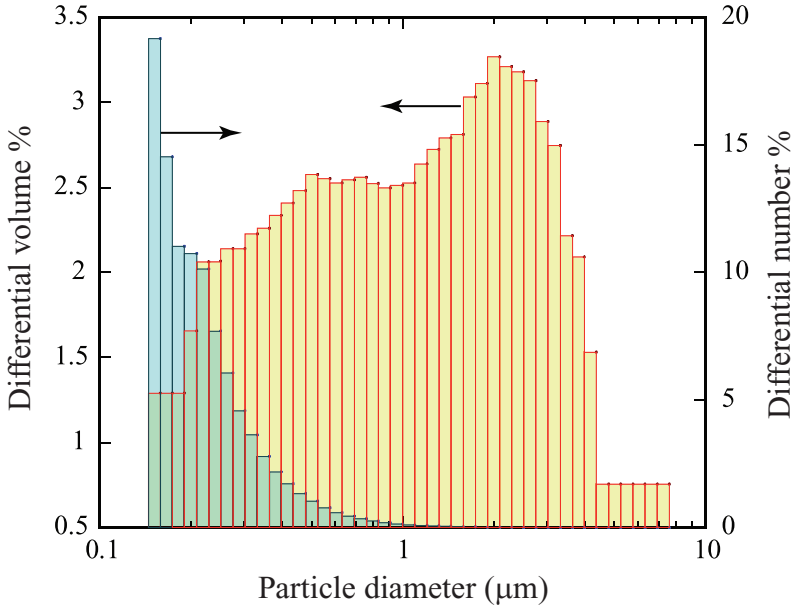

Figure 21: Particle size distribution of H.C. Starck HS boron carbide powder (year: 2000), based on tabulated size vs. vol% data published by the company (laser diffraction, Fraunhofer model). The powder was sub-micron when viewed on a number basis, but not when viewed on a volume basis. The manufacturer's specified specific surface areas of 12.0205 m^2/g translates to an average particle diameter of 0.2 μm.

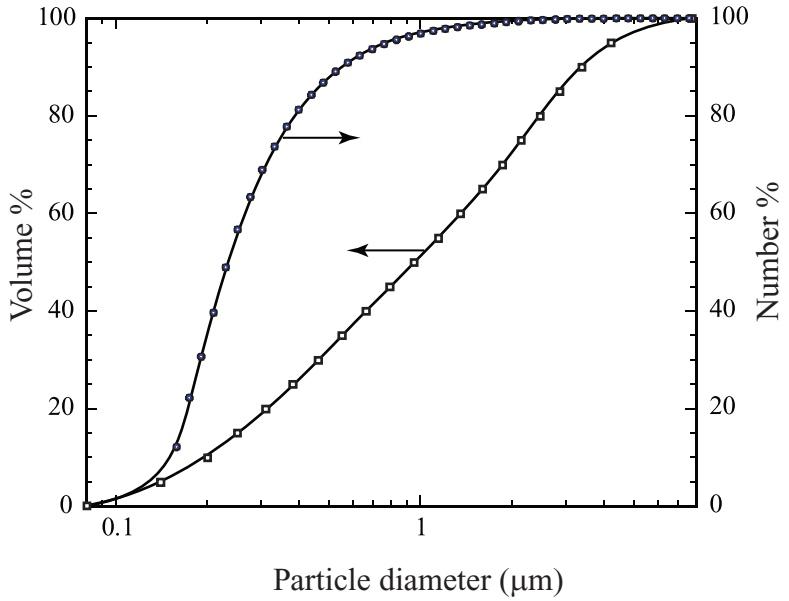

Figure 22: cumulative percent plot for Stark HS boron carbide powder (year: 2000) calculated tabulated size vs. vol% data published by the company (laser diffraction, Fraunhofer model)

In Figure 23, the thimble from a deflocculated suspension on the right sintered to a relative density of 94%, and had a uniform wall thickness. This specimen should be transformed to 100% relative density after post-HIPing. A solid cast specimen slightly larger than the 44.45% diameter pressed specimens sintered to 90% relative density (a 3% improvement is required). There is some indication from the cross section of the green part that the particle packing density near the center of the part was lower than near the surfaces.

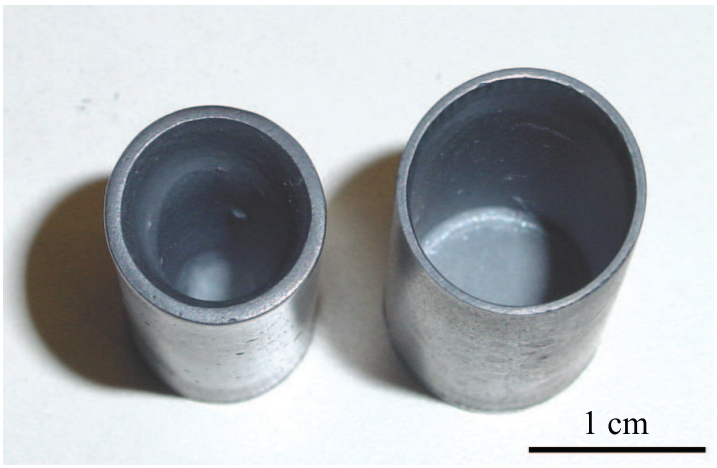

Figure 23: Slip cast thimbles from the same gypsum mold. Substantial shrinkage and non-uniform wall thickness is observed on the boron carbide thimble on the left because of an unstable suspension.

4.3 Sintering of Nano-sized Boron Carbide

4.3.1 Powder treatment

The phases of as-received and methanol washed nano-powder were identified by XRD. Figure 24 a and b show the XRD traces of as-received and three-times methanol washed PPG nano-powders from #8 to #16, respectively. XRD peaks show that the main phase of the as-received powders was crystalline boron oxide and glass phase (broad amorphous humps). After three times methanol washing, boron carbide (B_4C) appeared as the main phase. Based on the peak at 26.6° in 2θ, corresponding to the most intense peak of graphite, some free carbon was present in the methanol washed powder and the relative proportions depend on the powder processing conditions. Nano powders which were made by a process B shows higher carbon contents. In case of PPG #12, silicon carbide (SiC) was detected due to Si doping during powder processing.

Figure 25 shows the TEM micrographs and diffraction patterns of as-received and methanol-washed PPG #14 powder. Particles appear faceted and uniform. The selected area diffraction pattern from many particles shows significant reduction, but not elimination of amorphous content after methanol washing.

Figure 26 shows XRD traces of three-times methanol washed PPG nano-powder from #17 to #29. XRD peaks show that boron carbide (B_4C) is major phase with graphite as a secondary phase and also the graphite contents depended on the powder manufacturing process. Based on broadened B_4C peaks, liquid feed specimens yielded finer particles than with solid feed. SiC was detected for samples PPG #24 and #25 as a secondary phase. All samples appear to have a relatively high free graphite content.

Figure 27 shows microstructures of pressed pellets of PPG #8 and #13, which are made from process A, and #15 which are produced from process B. Micrographs with low magnification (left side) and high magnification (right side) showed that particle size distribution of process A is much wider than that of process B.

Weight changes during methanol washing were monitored by precise weight measurement for PPG #14 and PPG #21 in different containers which were beaker and vials, and the results of weight loss are shown in Figure 28. Weight losses were ∼55% and ∼45% for

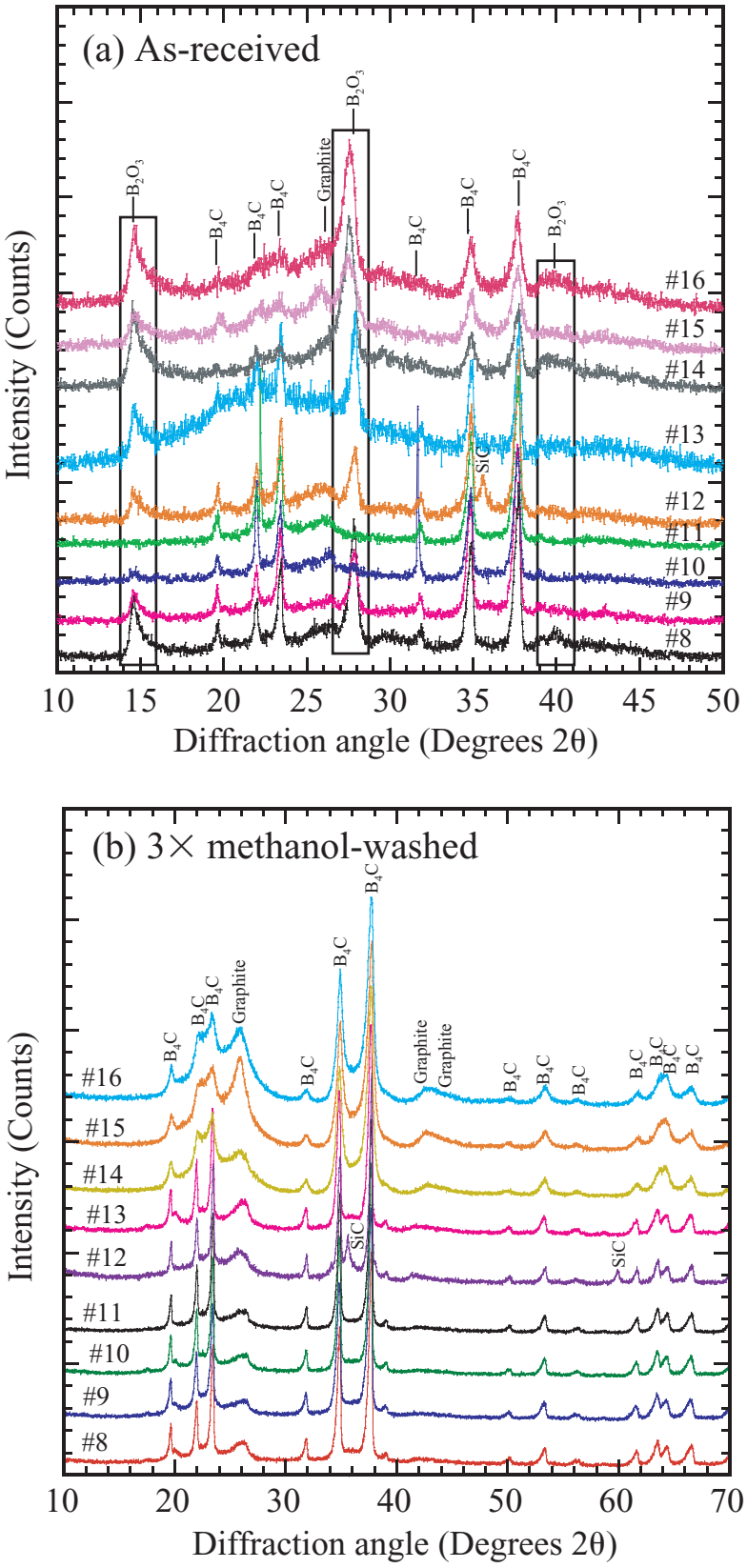

Figure 24: XRD peaks of (a) as received and (b) after 3× methanol washed PPG nano-powder.

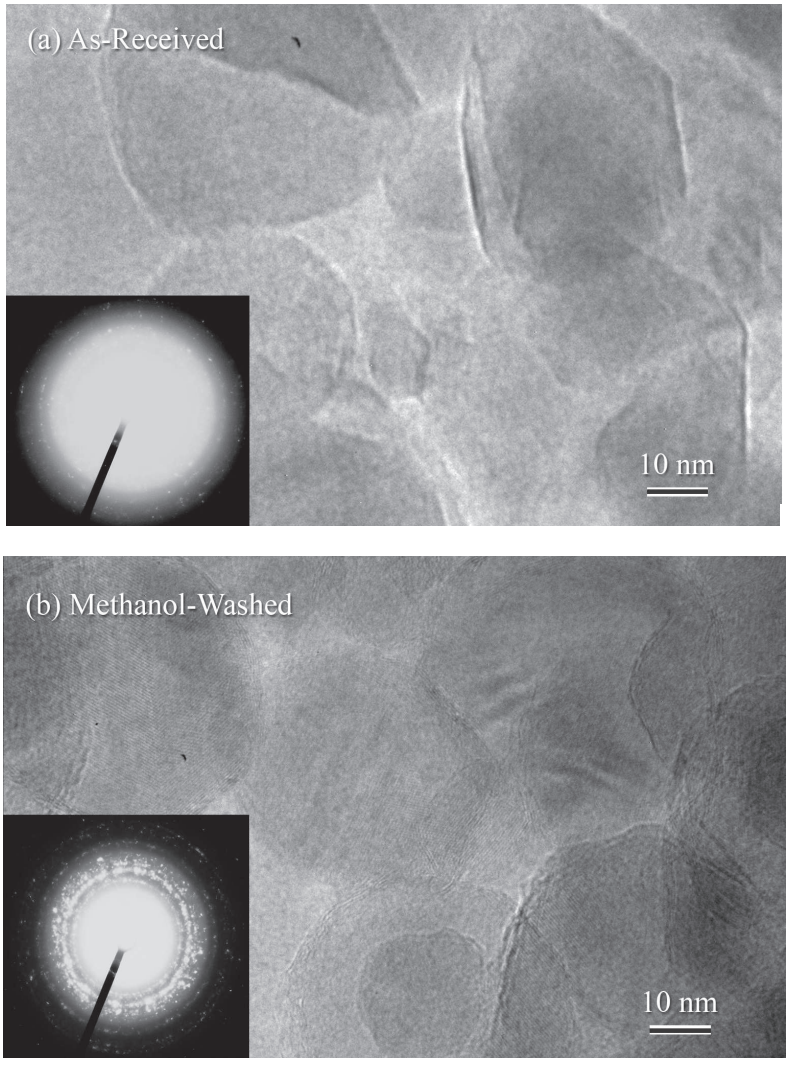

Figure 25: TEM micrographs and diffraction patterns of (a) as received nano-powder and (b) after methanol washing (courtesy of Y. Berta).

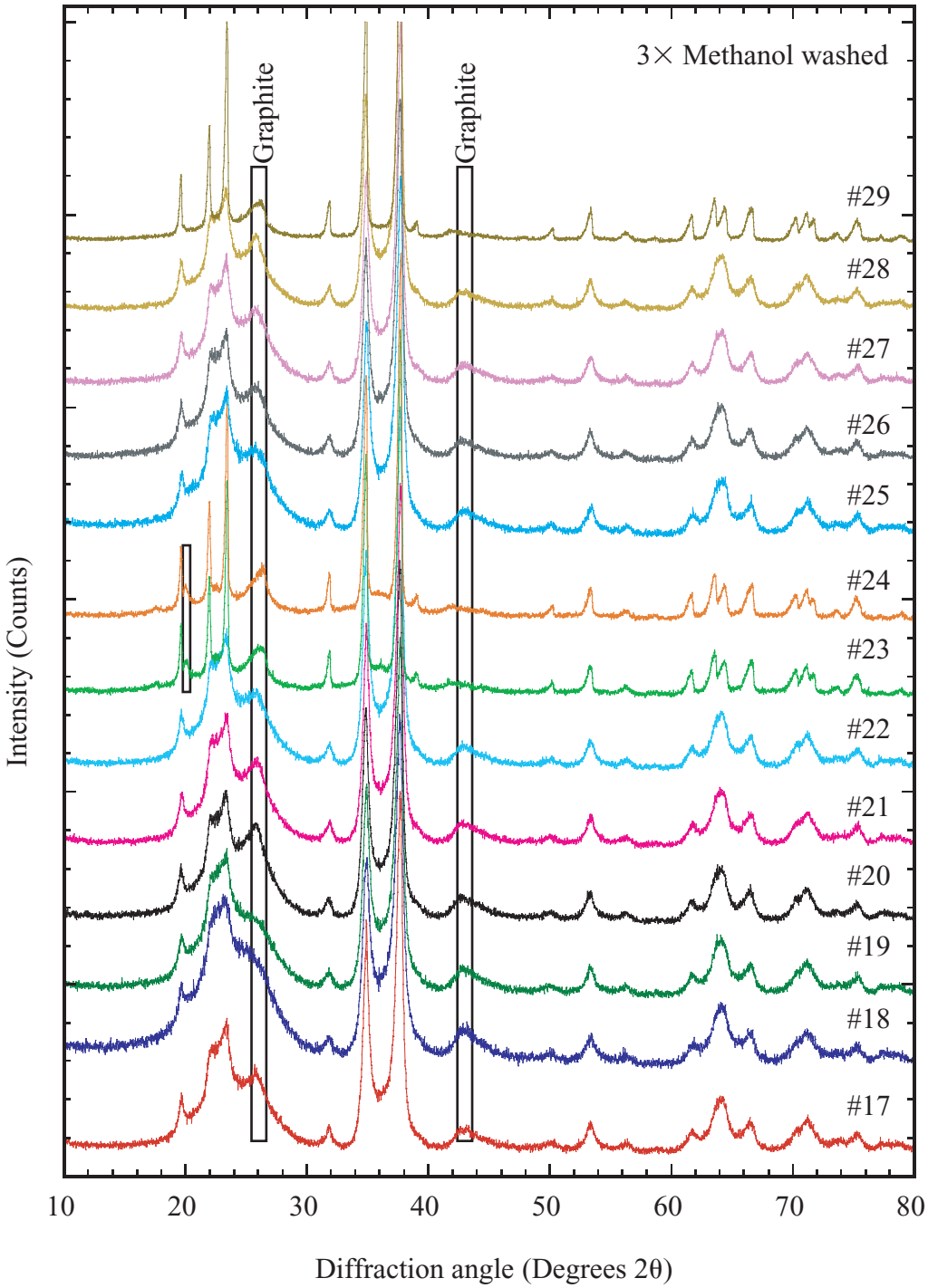

Figure 26: XRD traces of PPG nano-powder form #17 to #29 after 3× methanol washing. In all case, boron carbide (B_4C) was major phase with graphite as a secondary phase. Si doped samples (#23 and #24) show SiC peaks around 21° in 2θ as minor phase.

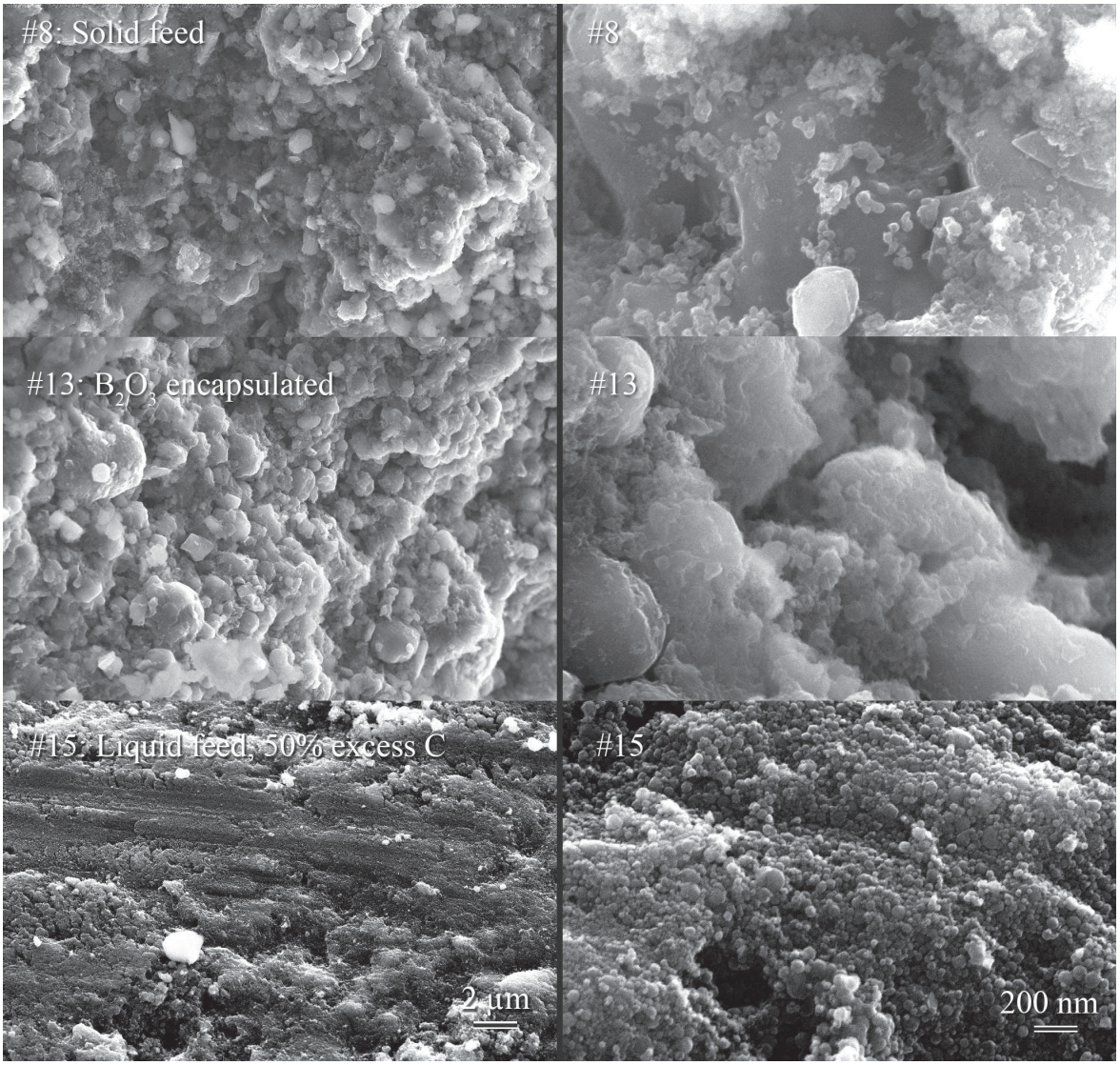

Figure 27: SEM micrographs of fractured surface of green body made by (a) PPG #8, (b) PPG #13 and (c) PPG #15.

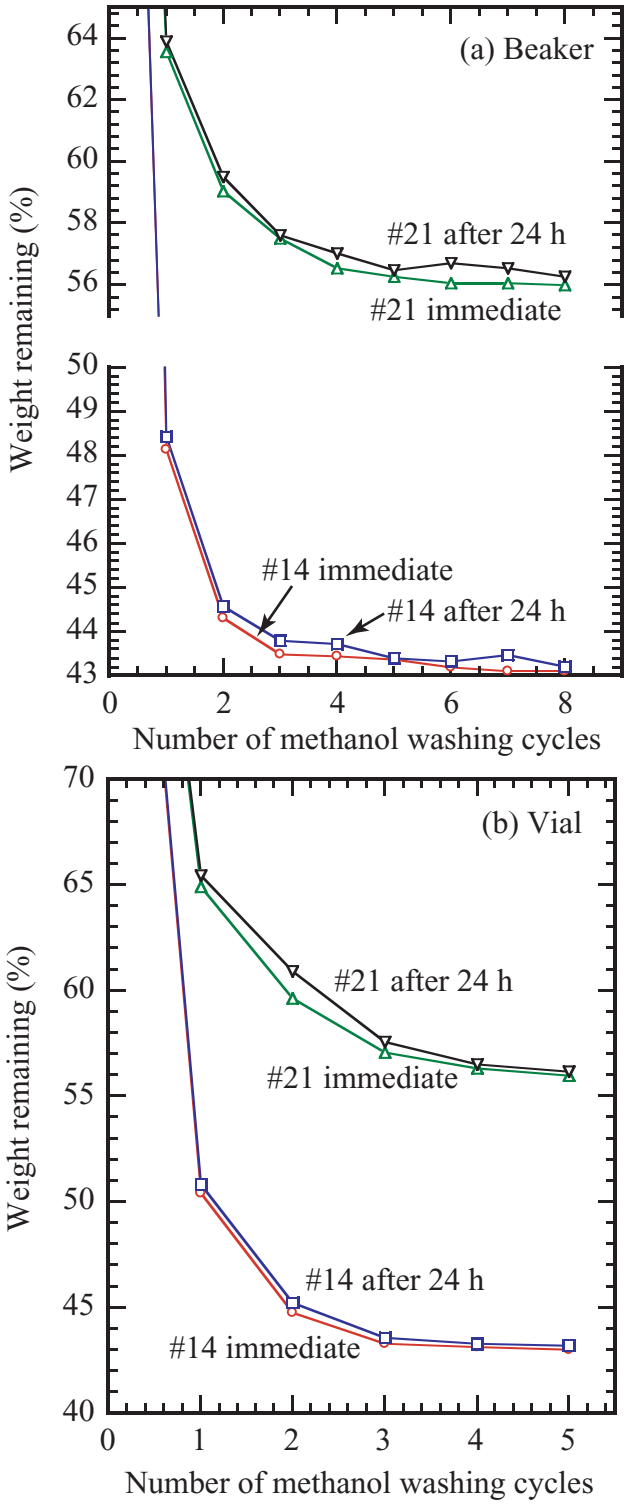

Figure 28: Weight change after repeated methanol washing cycles.

Table 4: Green and fired relative density and weight loss of PPG nano-powder from PPG #8 to # 16.

Composition	Comments	Weight loss (%)	Green relative density(%)	Fired relative density (%)
PPG # 8	Stoich.	12.9	61.9	71.6
PPG # 9	Ex B	10.8	64.5	72.1
PPG #10	+ N, Ex B	11.85	65.7	75.0
PPG #11	+ N	13.5	66.5	81.1
PPG #12	+ Si	22.3	64.6	64.3
PPG #13	B_2O_3 En.	18.5	63.1	83.1
PPG #14	Stoich.	5.2	68.5	95.2
PPG #15	50% ex C	4.6	65.7	91.8
PPG #16	60% ex C	5.5	66.9	94.4

PPG #14 and #21, respectively. After exposure to air for 24 h, slight weight gain were observed in both cases.

4.3.2 Sintering of Nano-powder

Figures 29 and 30 show the dilatometry traces of PPG nano-powders, which were 3× methanol washed, from process A and process B respectively. In case of process A powder, as shown in Figure 29, dimension changes slightly increased from room temperature up to 2110°C with fluctuation. After starting to rapid shrinkage at 2110°C, all process A samples showed single stage-shrinkage. The furnace was shut down at shrinkage rate was less than 0.005%/min. All the process A powder showed a relatively large weight loss during sintering, as shown in Table 4, and low fired relative density. In case of process B powder, as shown in Figure 30, a small hump is observed around 1325°C and started to sinter over 1575°C. Over 1700°C, rapid shrinkage was observed until ∼1900°C followed by plateau. Shrinkage re-accelerated over 2100°C, and then saturated. The weight loss was relatively small (∼5%) compared with the process A and showed higher fired relative density of over 90%.

Figure 31 shows the XRD traces after sintering for #8 to #16. In case of process A, major graphite peak, which in 26.6°, disappeared after sintering. In contrast, the major peak of graphite of sintered process B powder was increased.

The effect of residual boron oxide (B_2O_3) on sintering behavior was monitored by

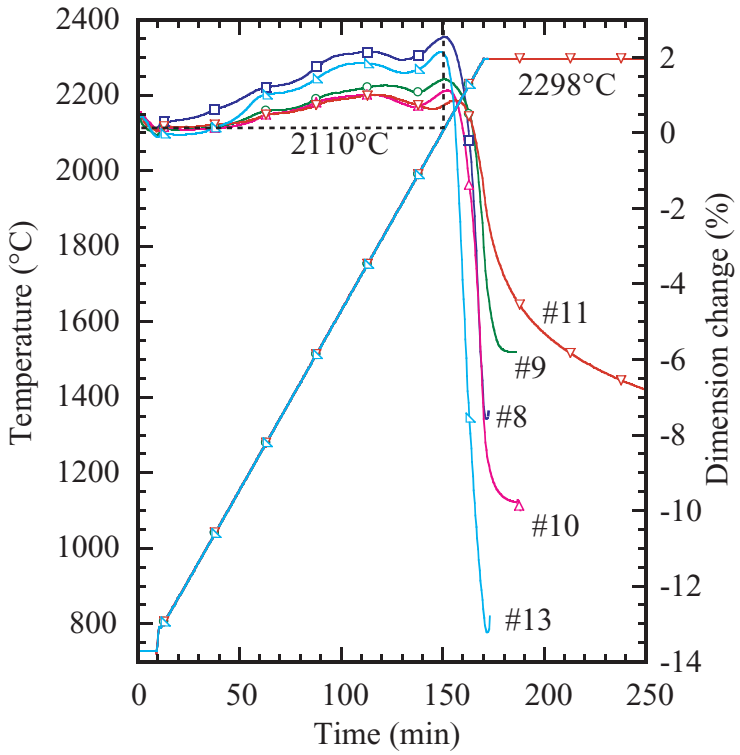

Figure 29: Dilatometry traces of nano-sized B_4C powder made from process A.

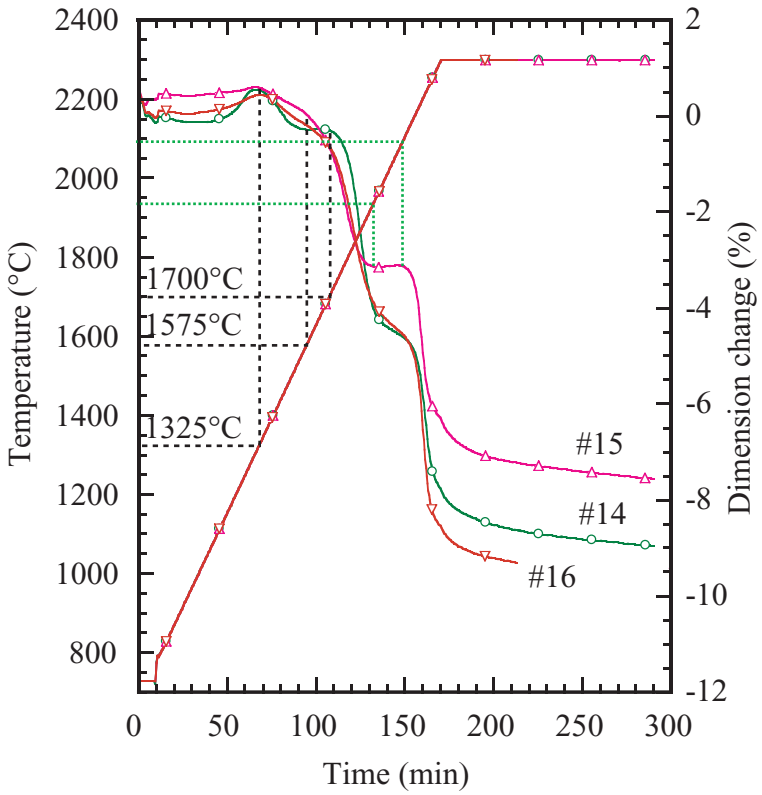

Figure 30: Dilatometry traces of nano-sized B_4C powder made from process B

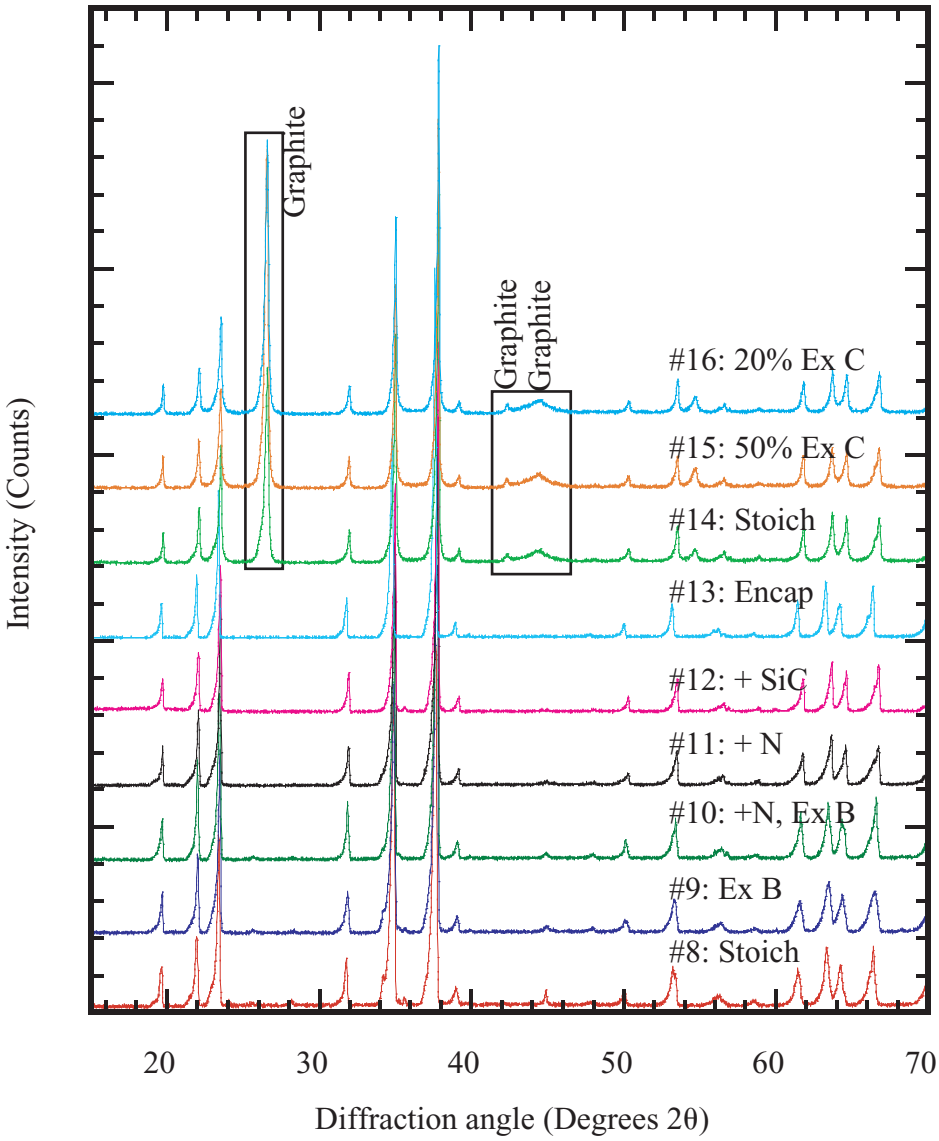

Figure 31: XRD peaks of sintered PPG nano powder form #8 to #15.

dilatometry. To remove residual boron oxide, PPG #14 powder was methanol washed multiple times or methanol washed followed by vacuum heat treatment, and then sintered at 2300°C with heating rate of 10°c/min. Figure 32 shows the dilatometric traces of PPG#14 powders with various B_2O_3 removal heat treatments. Sintering before the contraction plateau at 1900°C was more extensive as the B_2O_3 removal process was more aggressive.

Figurer 33 shows a dilatometric trace of low temperature soak to prevent the formation of nano liquid phase over 1990°C. Densification continued at a slow rate during the soak without particle coarsening as shown in Figure 34.

4.3.3 Sintering Behavior of PPG# 15

Figure 35 is a TEM micrograph of B_4C nano-particles which show distinct coatings with wide lattice spacings of 0.36 nm. Selected area diffraction patterns (not shown) displayed diffuse halos indicating amorphous material, as well as well-defined spots within the halos implying diffraction from crystalline material.

Specimen compacts were heated to various temperatures up to 2400°C, cooled, and then weighed after removing from the furnace, and then weighed again after exposure to room air for 24 h. As shown in Figure 36, weight losses were measured after immediate weighing of heat-treated specimens. Weight loss increased in extent from 967°C to ∼1537°C, showing no consistent trend at higher temperatures. Specimens weighed after exposure to room air showed weight gains from ∼967 to 1157°C, followed by weight losses at higher temperatures. There was no measured change in weight after exposure to room air for specimens heated to or above 2013°C.

Figure 37 shows a dilatometry trace in which an expansion hump was detected over the temperature range 1150-1450°C, followed by densification interrupted by an arrested contraction over a temperature range of 1850-2150°C. The volumes of specimens which were quenched every ∼100°C were determined by dimensional measurements; from this, dimensional relative densities are also plotted in Figure 37. The dimensional relative density behavior closely mirrors the dilatometry trace.

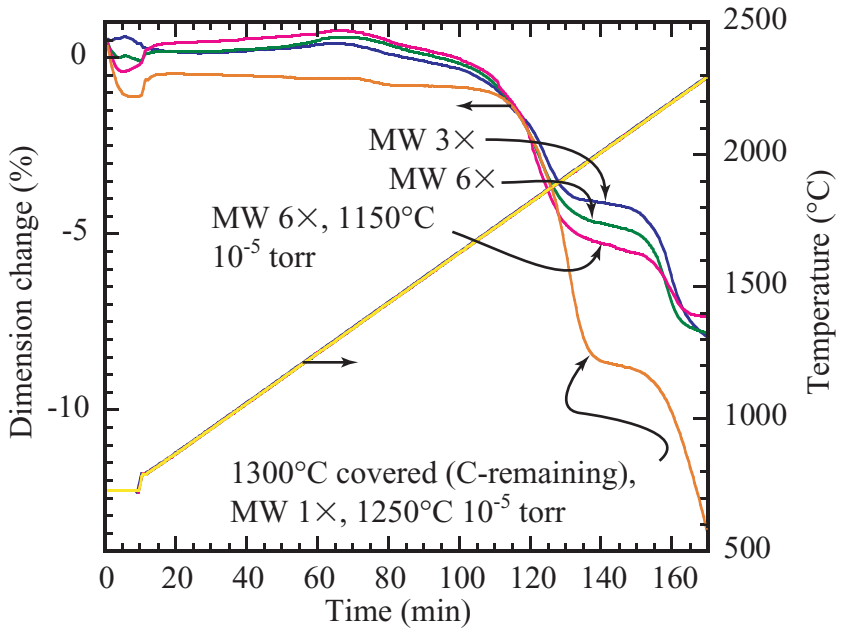

Figure 32: Dilatometry traces of four samples exposed to different B_2O_3 removal processes

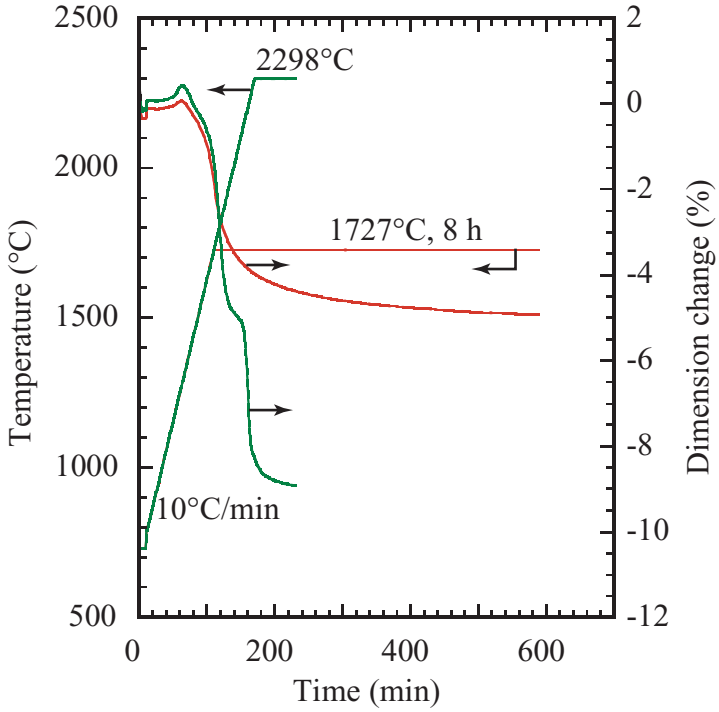

Figure 33: Dilatometric trace of low temperature soak to prevent the formation of nano liquid phase

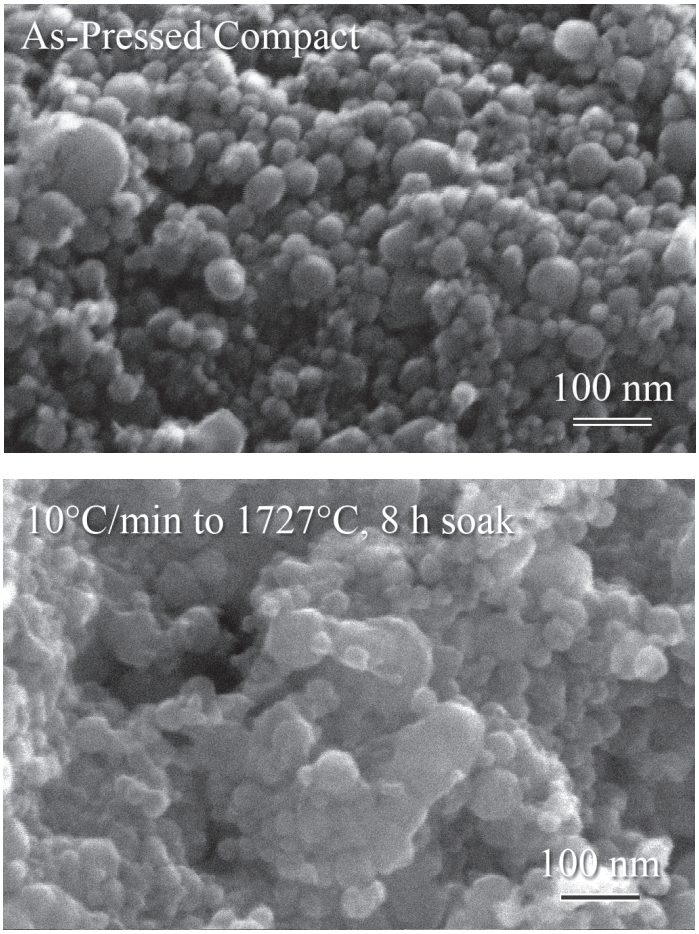

Figure 34: SEM micrographs of (a) as pressed PPG #14 and (b) after low temperature soak at 1727°C for 8 h.

Figure 38 shows XRD patterns of specimens quenched at various temperatures. Crystalline B_2O_3 was detected up to but not above 1252°C. B_4C peaks became increasingly deconvoluted at and above 1823°C. Based on relative intensities, the specimens consist of a substantial relative percentage of graphite. Graphite peak intensity increased and peak width decreased at and above 2203°C; the ratio of peak area at 2203°C to that at 2155°C is 1.35.

Figure 39 shows nano-particles of ∼20-40 nm in the early stages of sintering with increasing temperature up to 1918°C, without substantial changes in particle size. The specimen heat-treated to 776°C showed deviations from sphericity corresponding to crystal habit, which is representative of the methanol-washed starting powder.

Figure 40 shows a distinct change in morphology starting at 1918°C. The comparatively large grains in the micrographs corresponding to the temperature range 1918-2108°C appear as smooth fracture surfaces. These grains appear isolated and are of sizes at least an order of magnitude larger than the nano-particles. The appearance of this bimodal morphology at 1918°C corresponds to the onset of the region of slowed contraction in Figure 37.

Figure 41 shows specimens quenched at 2203 and 2298°C with large grains having smooth fracture surfaces, which are increased in size and appear interconnected. This change in microstructure starting at 2203°C corresponds well to the onset of renewed rapid contraction in Figure 37.

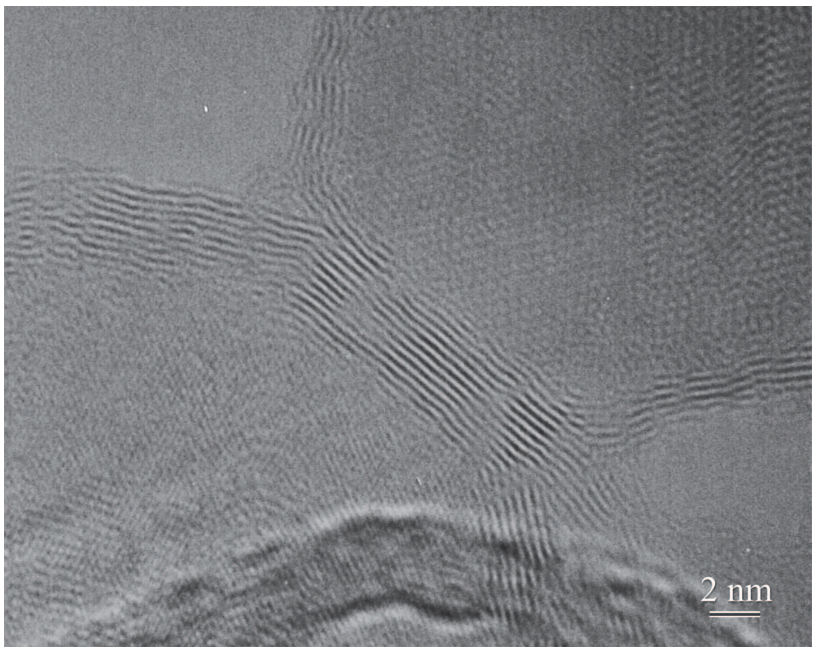

Figure 35: Transmission electron micrograph of methanol-washed B_4C particles with graphite exterior regions (see Discussion section).

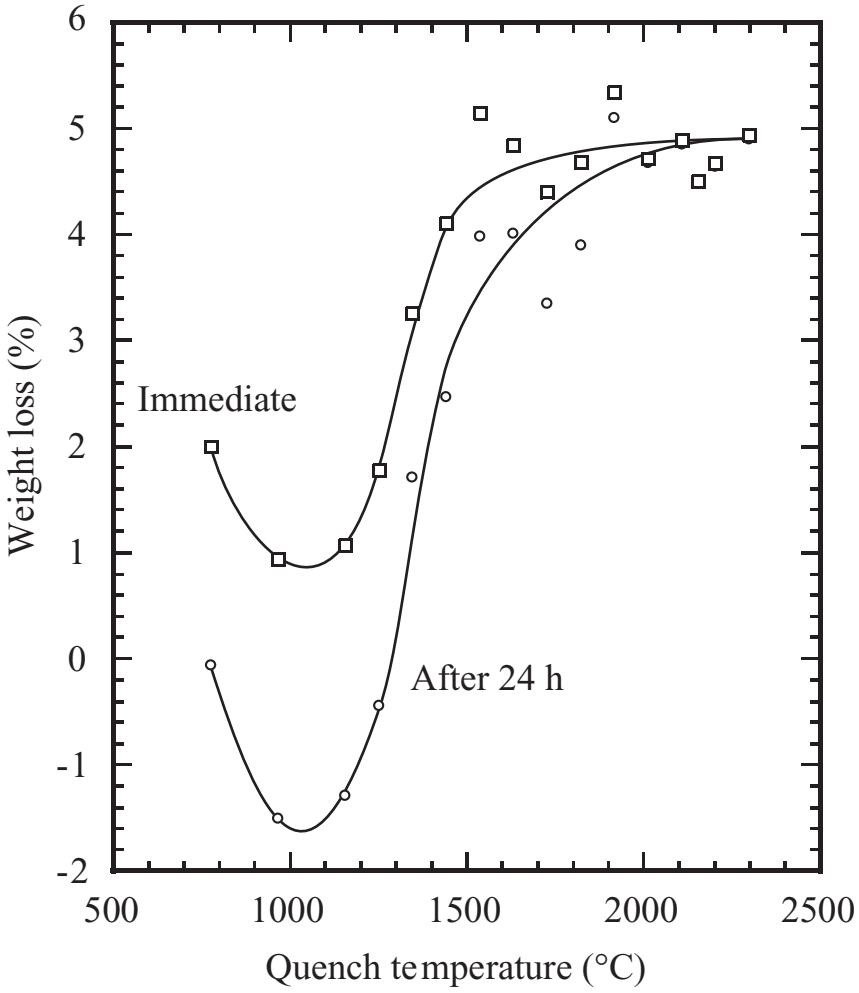

Figure 36: Weight changes of specimens heat-treated at 50°C to 800°C, and then 10°C/min to various (quench) temperatures, and then furnace-cooled with the heating elements turned off, both in flowing He. Specimens were weighed immediately as well as after exposure to ambient air for 24 h.

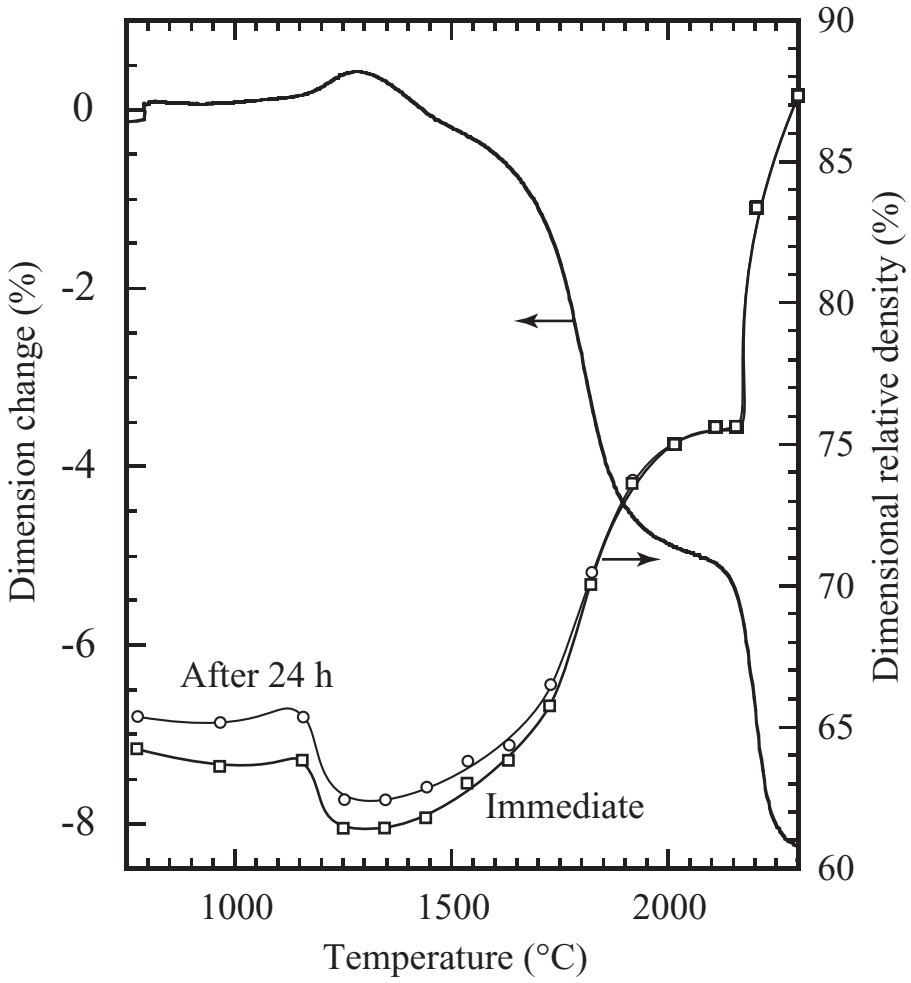

Figure 37: Dilatometry trace (10°C/min) of nano-B_4C powder compact as well as relative densities of specimens based on dimensional and weight measurements immediately after removal from the dilatometer and after exposure to room air for 24 h.

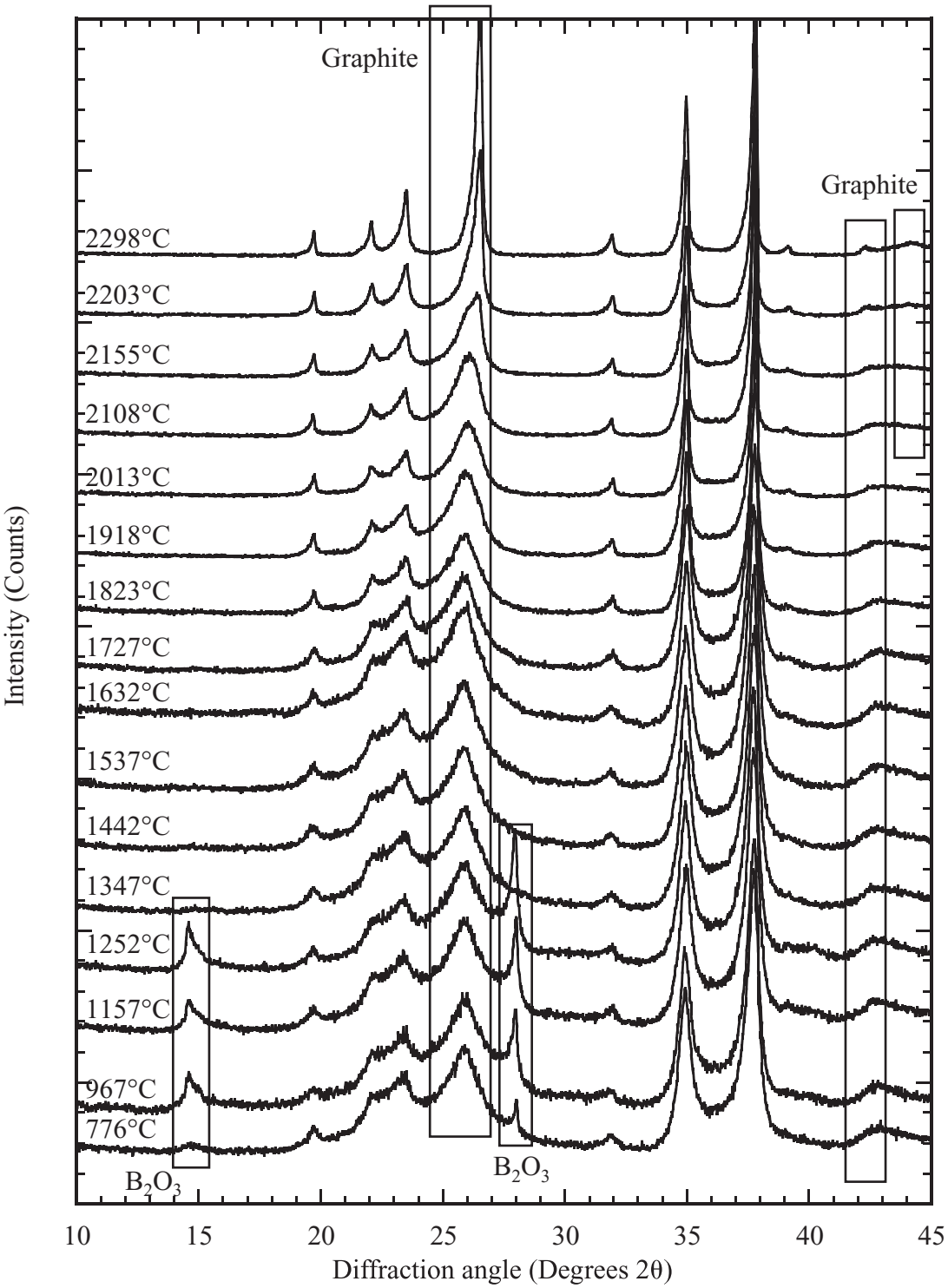

Figure 38: XRD traces of specimens heated at 50°C to 800°C, and then 10°C/min to various temperatures and quenched. All un-marked peaks correspond to boron carbide. International Committee for Diffraction Data (ICDD) numbers: 37-0798 for B_4C solid solution, 13-0570 for B_2O_3, and 75-2078 for graphite.

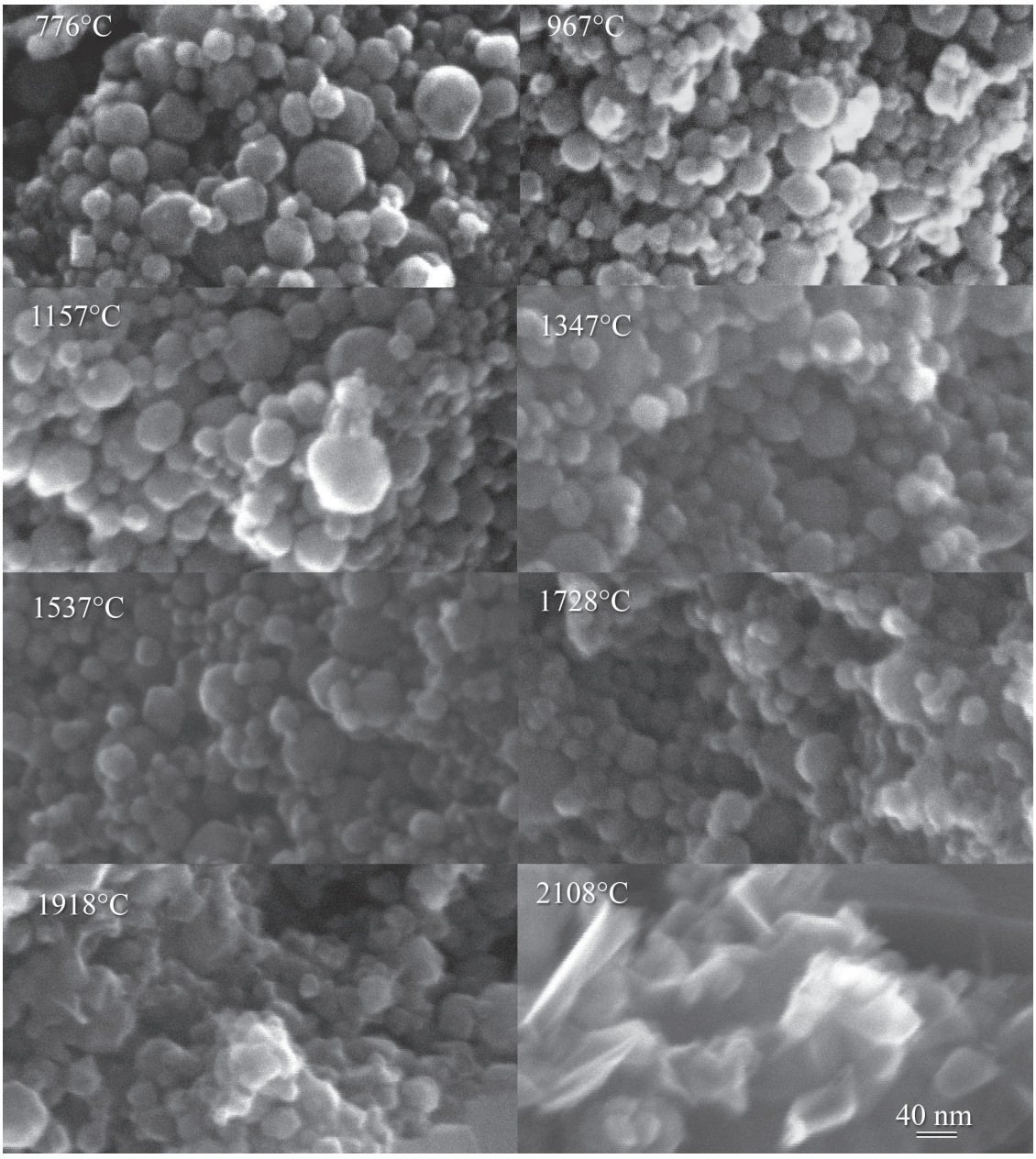

Figure 39: Secondary electron high-magnification SEM micrographs of selected regions of specimens heated at 10°C to the indicated temperatures.

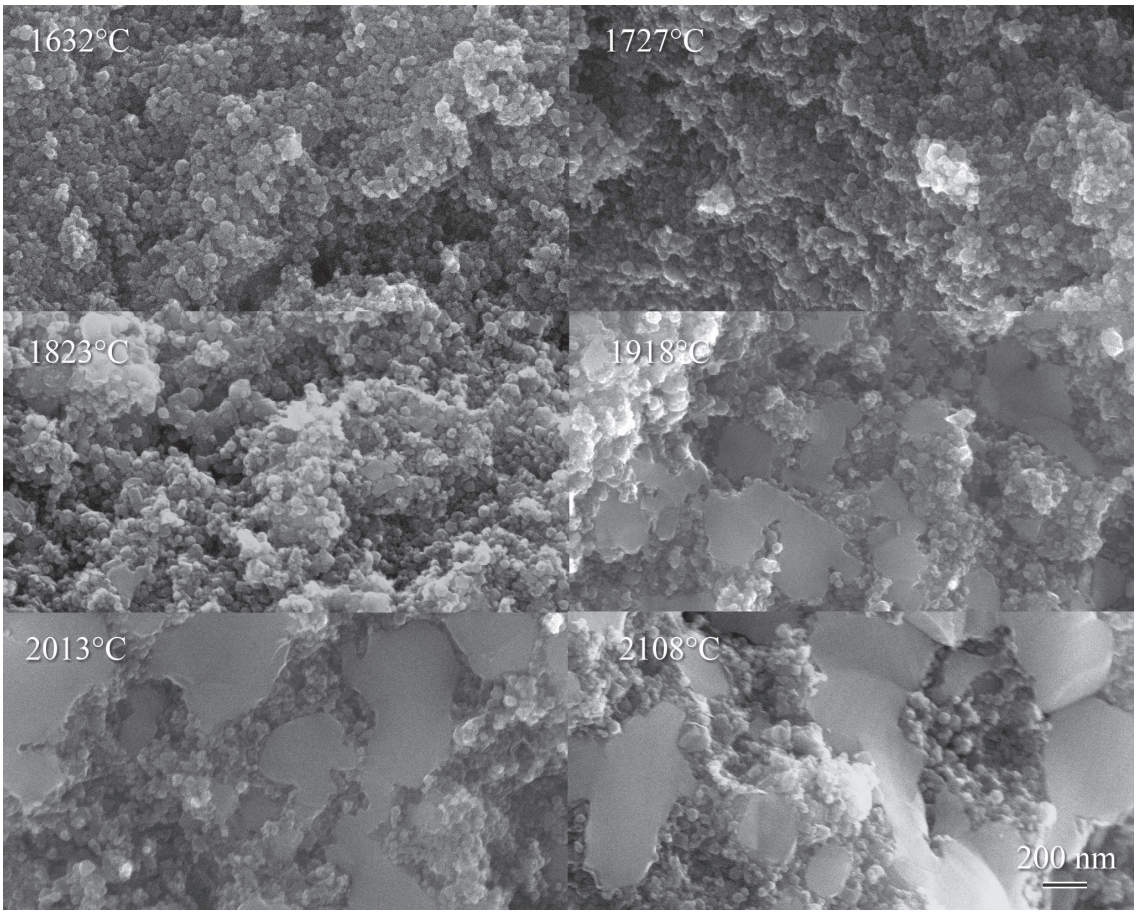

Figure 40: Secondary electron mid-magnification SEM micrographs of selected regions of specimens heated at 10°C to the indicated temperatures.

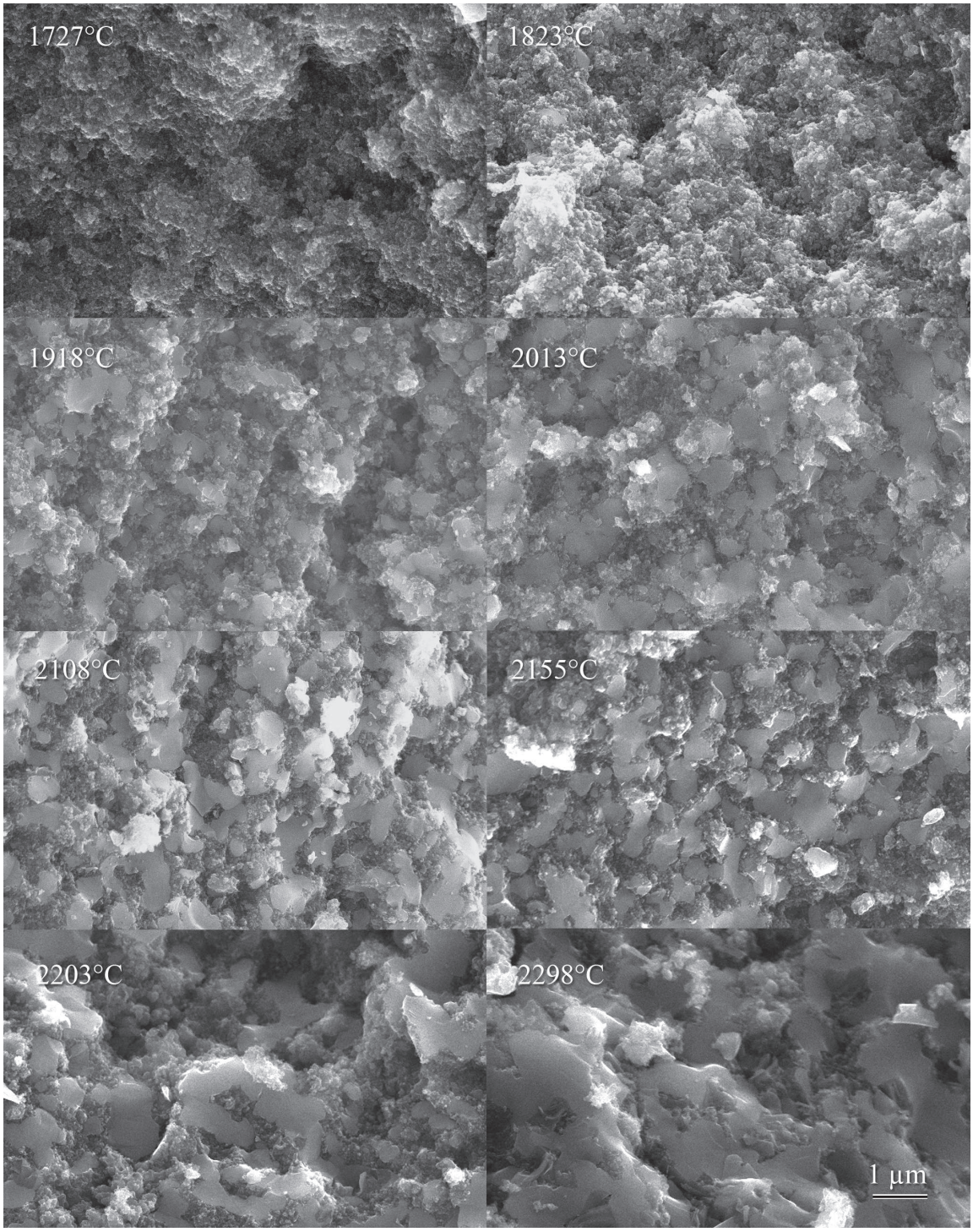

Figure 41: Secondary electron low-magnification SEM micrographs of selected regions of specimens heated at 10°C to the indicated temperatures.

CHAPTER V

DISCUSSION

5.1 Sintering Optimization

5.1.1 Stark Powder

In previous work [9] in our laboratory, the presence of B_2O_3 coatings on B_4C particles was inferred from weight loss data. Its presence in this study was confirmed directly from the XRD pattern of the green compact (Figure 11).

Soaking at 2298°C for times longer than the minimum required to reach the termination of densification precipitously degraded the relative density and Vickers hardness (Figure 12). These can be associated with exaggerated grain growth; the grain size after 150 min was an order of magnitude larger than that after 17.5 min. These large grains were the cause of the apparent preferred orientation effects in the XRD patterns (variations in relative intensities). As these grains grew, the original grain boundary porosity was likely dragged, accumulated, and discarded to form the large fissures decorating the slow-growth directions of the boundaries of the large grains (Figure 13c). The decrease in relative density implies some dilation of these pores/fissures, perhaps attributable to the pressure of trapped He or B_4C (or its molecular sub-units) vapor, or strains to accomodate exaggerated grain growth. The decrease in hardness is attributable to the increased grain size, decreasing the grain boundary area available for dislocation pinning [54], as well as the increased porosity. The increased scatter in hardness values with longer soak times is consistent with the coarser microstructure showing less uniformly distributed porosity, imposing more variability from indent to indent.

Vickers hardness increased in concert with relative density as the soaking temperature was increased up to 2251°C, as would be expected. Heat-treatment soak temperatures at and above 2317°C showed a degradation in relative density and Vickers hardness, concurrent with rapid grain growth, an increase in graphite concentration, and for the 2336°C soak

temperature, some form of decomposition of the B_4C phase. The increase in graphite content is consistent with our previous interpretation [9] that B_4C, especially at more elevated temperatures, forms a boron rich vapor, leaving carbon behind at the grain boundaries or triple points. It is also possible; however, that these temperatures permitted pre-existing amorphous carbon to devitrify to graphite. Similar to that which occurs with extensive soak periods at 2298°C, exaggerated grain growth at the higher soaking temperatures occurred (e.g. the bimodal grain size distribution of the specimen soaked at 2317°C in Figure 14). Unlike that which occurs with the extensive soak periods at 2298°C, extensive porosity was left within the large grains, and large fissures at the boundaries were not evident; higher temperatures enabled grain boundaries to more easily pull away from pores.

The faceted pores which were only observed in the commercial (uniaxially) hot-pressed B_4C (Figure 17) have been coined "negative crystals," since facets are aligned with specific crystallographic planes of the grain. It is speculated that grains which suffer these negative crystals were originally particles which were wedged into poor fit with their neighbors prior to uniaxial hot pressing. Their extensive deformation, partly resulting from plastic flow and partly from sintering diffusion, to conform with neighboring particles, required extensive shear deformation which was accommodated by formation of these internal cavities.

The density of commercial hot-pressed B_4C was higher than densities obtained via pressureless sintering, but the Vickers hardness values (for soaking temperatures in the range 2203-2317°C) were the same within experimental error (Figure 15). Higher graphite concentration (Figure 11), slightly higher average grain size (Figure 14), and well dispersed fine porosity (negative crystals) of the commercial hot-pressed specimen, may all have contributed to the lowering of the Vickers hardness of the commercial hot-pressed B_4C to the range of the pressureless sintered specimens, which had a comparatively higher concentration of porosity.

Sintered densities were higher with higher green densities (Table 3). For the larger specimens, CIPing was required to achieve uniformity in particle packing in the green state, to in turn form crack-free sintered parts. Post-HIPing of pressureless sintered specimens was remarkably beneficial to relative density and hardness, for specimens which had pressureless

sintered to closed porosity (>93% relative density). The absence of pull-outs in micrographs of post-HIPed specimens (e.g. Figure 14) implies that pull-outs in other micrographs (e.g. Figure 13a) are associated with grains with adjacent grain boundary porosity. Post-HIPing did not change the nature of the B_4C phase (based on XRD), and the relative density and Vickers hardnesses were markedly higher than those of commercial hot-pressed B_4C. Unlike hot-pressing, a part may be cast (e.g. slip cast) into a complex shape, pressureless sintered and post-HIPed, with that shape retained.

5.1.2 PPG Nano-Powder

The starting powder after methanol-washing is viewed as nano-particles in which methanol washing has removed the majority of encapsulating B_2O_3. The boron oxide remaining after methanol-washing is speculated to be in regions in poor contact with the liquid, such as in the interiors of particle agglomerates. The remaining B_2O_3 was detected both in the crystalline form (based on Figure 38) and the amorphous form (based on the amorphous rings in TEM selected area diffraction patterns and weight loss measurements).

The rapid weight losses in the range 1157-1442°C (Figure 36) was shown previously to be volatilization of B_2O_3 (crystalline B_2O_3 melts at 450°C and boils, i.e. has a 1 atm vapor pressure, at ∼1860°C [55]). Low-temperature heat treatments, which do not remove B_2O_3, appear to increase the propensity at its surface for adsorption of atmospheric moisture (presumably working toward forming boric acid, H_3BO_3). Based on no atmospheric absorption being measured for specimens heat treated to 2108°C and above, it is inferred that B_2O_3 had been eliminated. The presence of B_2O_3 on the particles was not anticipated after three methanol washing cycles; this method is effective at removing much, but not all, of the boron oxide encapsulating the B_4C nano-particles. The indicated elimination of crystalline B_2O_3 peaks at and above 1347°C from Figure 38 is in contrast to the persistence of B_2O_3 to higher temperatures implied by Figure 36. For quench temperatures at and above 1347°C, the enduring B_2O_3 converted from liquid to glass when cooling to room temperature (or the remaining crystalline portion was of a volume lower than that detectable by XRD).

The coatings on the nano-particles with comparatively wide lattice spacings is interpreted to be graphite [56], which has a (002) d-spacing of 0.34 nm (ICDD: 37-0798), which is close to the 0.36 nm spacing measured from Figure 35. Using as an estimate, a particle sphere (B_4C + C) outer diameter of 42.5 nm and a particle sphere minus carbon coating diameter of 34.1 nm, there is a ~1:1 B_4C:C volume ratio. This is consistent with the large relative intensity of the most intense graphite peak in Figure 38 compared to B_4C peaks.

The temperature range in which B_2O_3 was predominantly thermally extracted in Figure 36 (1157-1442°C) corresponds well to the expansion hump in the dilatometry trace (Figure 37). The expansion corresponds to specimen bloating as a result of rapid escape of B_2O_3 vapor from the compact, and the contraction recovery after the hump maximum corresponds to particles collapsing together into the space left behind by the extracted oxide.

The onset of sintering is ~1500°C, which is lower than that observed for the $d_{50} = 0.8$ μm scale pure B_4C powder compacts in our previous work (1840°C), but higher than the 1380°C onset observed for carbon-doped (via phenolic resin) B_4C $d_{50} = 0.8$ μm powder compacts (in which the carbon reacted with and removed B_2O_3 coatings on particles). Thus, the substantially lowered onset of sintering anticipated for nano-scale powder compacts was not realized. One likely cause of the delayed sintering onset was the presence of B_2O_3, keeping the graphite-coated particles separated. Even after volatilization of those coatings, the particles in contact were graphite-coated B_4C. As a general rule, the onset of sintering increases with increasing melting temperature of the particles to be sintered. Since graphite is considerably more refractory than B_4C, contacting graphite-coated B_4C particles would likely start sintering at temperatures higher than pure B_4C particles in contact.

The arrest in contraction starting at ~1850°C corresponds to the formation of larger (~0.2-0.5 μm) grains, interpreted to have been liquid, given their smooth appearance. This is unexpected given that the B_4C-C phase diagram [2] indicates a B_4C-C eutectic at 2375-2400°C. It is interpreted that the high surface energy associated with the nano-powder shifted the eutectic melting temperature of the intimately-contacting B_4C and graphite to ~1900°C in which isolated liquid droplets formed from the fusion of a region of neighboring

nano-particles. Since these droplets were of an order of magnitude or more in scale than the nano-particles, it is interpreted that they quickly resolidified (while exposed to continued heating). This is supported by the non-wetting, isolated appearance of these grains in the microstructure. The arrest in densification measured starting at ~1900°C is the opposite of what would be expected as a result of liquid phase formation. However, by forming large-grained regions which are only momentarily liquid, those regions would draw away from the surrounding nano-particles, forming a vast number of air-gaps which would inhibit sintering, or mask detection of local sintering, by the dilatometer.

The resumption of rapid contraction starting at ~2200°C corresponds to the formation of a much coarser liquid phase which is substantially interconnected. It is interpreted that this liquid remained as temperature increased. This liquid formed below the 2375-2400°C eutectic indicated by the Thevenot phase diagram [2], perhaps the result of additional impurities (not detected by XRD) which lowered the eutectic temperature. An older phase diagram [57]; however, does indicate a 2160°C eutectic at 30 wt% carbon, which is consistent with the formation of liquid phase in this study. This continuous liquid phase facilitated rapid densification via capillary action drawing liquid into open pores, or simply facilitated specimen slumping.

SEM micrographs imply that fracture occurred through liquid phase-inspired grains, which represent solidified liquid of what was B_4C and a substantial amount of graphite; upon solidification, a eutectic microstructure of these two phases would be expected. The fracture surfaces are thus likely within and along weak graphite lamella, which explains why fracture of a microstructure in the early stages of sintering would occur through the large grains as opposed to around them. The graphite XRD peak at ~26° 2θ became notably sharper and of greater intensity for specimens heat treated to 2203 and 2298°C. While in the liquid, it is interpreted that the vapor pressure of the boron constituent of the liquid was substantially higher than the carbon constituent. Upon solidification, the proportion of graphite to boron carbide would then be higher than in nano-particles which initially fused to form the liquid phase. Since liquid was formed only momentarily for microstructures up to 2155°C, no increase in graphite content would be detected. However,

at and above 2200°C there was time for volatilization from the liquid phase, resulting in the higher detected graphite content.

5.2 Green Body Optimization

The oxidation behavior of boron carbide at moderate temperature was investigated by thermogravimetry. Based on Williams and Hawn, a sharp weight loss between 50°C and 125°C corresponds to removal of adsorbed water on particle surface. A more gradual weight loss between 150°C and 350°C may be a dehydration process which can be described as follows [50].

$$B(OH)_3 \rightarrow HBO_2 \rightarrow B_2O_3$$

Above 450°C, the temperature at which boron oxide melts, a large weight gain is observed corresponding to oxidation of B_4C: B_2O_3 are non-passivating coating.

$$B_{4(s)}C + 4O_{2(g)} \rightarrow 2B_2O_{3(l)} + CO_{2(g)}$$

The tendency of boron carbide to oxidize in air is an important consideration for processing. If organic binders, lubricants, polyelectrolyte dispersants, etc. are used, it would be desirable to burn them off in air, rather than allow them to leave residual carbon behind during heat treatment in helium/hudrogen. Further, it would be potentially useful, if feasible, to burn off the free carbon present in the powder in advance of sintering heat treatment.

Significant progress on slip casting has already been made by following the work by Williams and Hawn. However, slip cast green densities are still not as high as those obtained from CIPing. A systematic study for various solids loadings, of the viscosity versus pH, should quantify the best deflocculation conditions using electrolytic salt additions. A similar study using polyelectrolyte additions, e.g. Darvan, Tamil, etc., is merited.

5.3 Sintering of Nano-sized Boron carbide

5.3.1 Powder treatment

The phases of as-received and methanol-washed nano-powder were identified by XRD. Figure 24 shows the XRD traces of as-received and three times methanol washed PPG nano-powder from #8 to #16. Figure 24 a shows that main phase of as received powder was crystalline boron oxide and glass phase. The peak to noise ratio and the broad amorphous humps imply a significant concentration of amorphous materials. PPG #13 appeared to have the highest concentration of amorphous material. All samples showed some indication of crystalline graphite based on a broadened peak of low intensity. Figure 24 b shows XRD results for these powders after methanol washing. The peak to noise ratio is improved, implying that a substantial percentage of amorphous material was removed, likely amorphous B_2O_3. There is no indication of crystalline B_2O_3 after methanol washing. The presence of graphite is clearly seen for all samples. However the concentration of graphite relative to boron carbide is substantially higher for PPG #14 to #16, which are produced from process B. The boron carbide peaks for PPG #14 to #16 were significantly broadened, indicating nano-scale powder. The graphite peak was broadened relative to the boron carbide peaks for PPG #8 to #14.

XRD traces of methanol-washed samples PPG #17 through PPG #29 are shown in Figure 26. Based on broadened B_4C peaks, process B specimens yielded finer particles than with process A. SiC was detected for samples PPG #24 and PPG #25 as secondary phase. All samples appear to have a relatively high free graphite content. It appears that BET data is in opposition to the broadening effects shown in XRD, since samples with a large surface area, e.g. PPG #29, had narrow, sharp B_4C peaks. This is likely from an amorphous B_2O_3 would result in comparatively low surface area detected by BET analysis, while XRD line broadening would remain sensitive to the actual B_4C particle size.

The weights change during methanol washing is shown in Figure 28. As can be seen form Figure 28, the behavior of the powders was similar in the two containers. Specimen PPG #14 lost more weight with each cycle than specimen PPG #21. Specimen PPG #14 reached a terminal weight after three washings, while this occurred for PPG #21 after six

washings. There was a distinct attenuation in the extent of weight loss with each subsequent cycle in all cases. Slight weight gains were observed after exposure to room air for 24h; no measurable variation in the extent of weight gain was discernable with the the number of cycle.

5.3.2 Sintering of Nano Powder

Figure 32 shows dilatometry traces (heating rate: 10°C/min) for three samples of uniaxially pressed powder compacts. One powder was methanol washed three times, the second and third were methanol washed six times. The third powder was further process by soaking a powder compact at 1150°C for 5 h in high vacuum ($\sim 10^{-5}$ torr). The bloating at ∼1300°C associated with B_2O_3 volatilization remained irrespective of the extra efforts to remove the oxide. However, leading up to the liquid phase induced pause in contraction at ∼1900°C, sintering was more rapid and extensive with increased washing repetitions and with the oxide volatilization treatment.

Based on available evidence, there appear to be two important impediments to sintering PPG nano B_4C powder compacts, boron oxide and free carbon. Boron oxide appears to stubbornly remain even after the efforts enumerated above to eliminate it from the powder, and is postulated to be a contributing factor in forestalling the onset of sintering until it volatilizes away. It is also possible that the carbon coverings on boron carbide particles forestall the onset of sintering since graphite is substantially more refractory than boron carbide (i.e. the onset of sintering for graphite particles would be expected to be higher than for boron carbide). Starting at ∼1900°C, the nano-induced eutectic between boron carbide and graphite sets an upper temperature limit to solid state sintering. Elimination of the graphite coatings may shift liquid phase formation to higher temperature.

CHAPTER VI

CONCLUSIONS

Using the hydrogen-based B_2O_3 removal/fast heating rate method developed previously, pressureless sintered relative density was increased from 94.7 to 96.7% by optimizing the soak temperature and time. Soaking times longer than those required for near-termination of densification (i.e. shrinkage rates less than 0.005%/min) resulted in degradation in relative density and hardness via increases in grain size and porosity. Heat treatment at and above 2317°C resulted in exaggerated grain growth, decreased relative density, increases in graphite concentration, and after soaking at 2336°C, decomposition of the B_4C phase. Post-HIPing pressureless sintered B_4C did not result in changes in the B_4C structure or concentration of graphite, and imbued substantial improvement to relative density (e.g. 100.0%) and Vickers hardness, so long as the pressureless sintered density was greater than 93.0%. In comparison to a commercial hot-pressed B_4C specimen, optimized pressureless sintered relative densities were lower, but the Vickers hardnesses were comparable. Post-HIPed pressureless sintered B_4C specimens had higher relative densities, lower graphite contents, and significantly higher Vickers hardnesses than commercial hot-pressed B_4C.

Nano-scale (20-40 nm) particles consisted of B_4C coated with graphite to form a ∼50:50 volume percent compositional mixture. Methanol washing was effective at removing much but not all of B_2O_3 encapsulation of these particles; the remainder of the boron oxide volitalized by ∼1500°C, which was the onset of solid state sintering. Isolated spherical ∼0.3 μm grains appeared in micrographs starting at 1918°C, which were interpreted to be from a momentary eutectic liquid, induced to form at lower than expected temperatures because of the contribution of high surface energy nanoparticles. Upon formation, these regions are interpreted to have quickly solidified into a eutectic microstructure of B_4C and graphite which easily fractured at room temperature. The gaps in particle packing facilitated by formation of these solidified liquid droplets impeded continued solid state sintering. Starting

at 2200°C, the formed liquid phase remained as liquid, which became interconnected and caused densification by capillary action of the liquid into void space, and/or caused compact slumping.

REFERENCES

REFERENCES

[1] J. F. Shackelford and W. Alexander, *CRC Materials Science and Engineering Handbook*, CRC Press, Boca Raton, Fl., 1991.

[2] F. Thevenot, "Boron Carbide-A Comprehensive Review," *J. Euro. Ceram. Soc.*, **6** [4] 205-225 (1990).

[3] D. Emin, "Structure and Single-Phase Regime of Boron Carbides," *Phys. Rev. B*, **38** 6041-55 (1988).

[4] V. Skorokhod Jr., M. D. Vlajic, and V. D. Krstic, "Mechanical Properties of Pressureless Sintered Boron Carbide Containing TiB_2 Phase," *J. Mater. Sci. Lett.*, **15** [15] 1337-39 (1996).

[5] C. H. Lee, C. H. Kim, "Pressureless Sintering and Related Reaction Phenomena of Al_2O_3-doped B_4C," *J. Mater. Sci.*, **27**, [23] 6335-340, (1992).

[6] Y. Kanno, K. Kawase, and K. Nakano, "Additive Effect on Sintering of Boron Carbide," *J. Ceram. Soc. Jpn.*, **95** [11] 1137-40 (1987).

[7] Z. Zakhariev and D. Radev, "Properties of Polycrystalline Boron Carbide Sintered in the Presence of W_2B_5 without Pressing," , *J. Mater. Sci. Lett.*, **7** [7] 695-96 (1988).

[8] K. Schwetz and G. Vogt, "Process for the Production of Dense Sintered Articles of Boron Carbide," U.S. Patent 4,195,066 (1980).

[9] H. Lee and R. F. Speyer "Pressureless Sintering of Boron Carbide," *J. Am. Ceram. Soc*, **86** [9] 1468-1473 (2003).

[10] H. Lee, W. S. Hackenberger, and R. F. Speyer, "Sintering of Boron Carbide Heat-treated with Hydrogen," *J. Am. Ceram. Soc.*, **85** [8] 2131-2133 (2002).

[11] N. Cho, Z. Bao, and R. F. Speyer, "Density- and Hardness-optimized Pressureless Sintered and Post-hot Isostatic Pressed B_4C," *Journal of Materials Research*, **20** [8] 2110-16 (2005).

[12] R. S. Averbak, H. J. Hofler, H. Hahn, and J. C. Logas, "Sintering and Grain Growth in Nanocrystlaline Ceramics," *Nanostructured Materials*, **1** [2] 173-8 (1992).

[13] O. Vasylkiv, Y. Sakka, and V. V. Skorokhod, "Low-temperature Processing and Mechanical Properties of Zirconia and Zirconia-Alumina NanoCeramics," *J. Am. Ceram. Soc.*, **86** [2] 299-304 (2003).

[14] D. L. Bourell, Parimal, and W. Kaysser, "Sol-gel Synthesis of Nanophase Yttria-stabilized Tetragonal Zirconia and Densification Behavior Below 1600 K," *J. Am. Ceram. Soc.* **76** [3] 705-11 (1993).

[15] J. R. Groza and R. J. Dowding, "Nanoparticulate Materials Densification," *Nanostructured Materials*, **7** [7] 749-768 (1996).

[16] B.-N. Kim, K. Hiraga, K. Morita, and S. Sakka, *Nature*, **413** [6853] 288-91 (2001).

[17] X. Xu, T. Nishimura, N. Hirosaki, R.-J. Xie, Y. Yamamoto, and H. Tanaka, "Superplastic Deformation of Nano-sized Silicon Nitride Ceramics," *Acta Materialia*, **54** 255-262 (2006).

[18] R. W. Rice, "Effects of Environment and Temperature on Ceramic Tensile Strength-grain Size Relations," *Journal of Materials Science*, **32** [12] 3071-87 (1997).

[19] H. Chang, J. Hofler, C. Alstetter, R. Averbak, "Synthesis, Processing and Properties of Nanophase Aluminide," *Materials Science and Engineering A*, **153** [1-2] 676-8 (1992).

[20] E. J. Gonzalez, B. Hockey, and G. J. Piermarini, "High Pressure Compaction and Sintering of Nano-size Gamma-Al_2O_3 Powder," *Materials and Manufacturing Processes*, **11** [6] 951-67 (1996).

[21] M. Wolff, A. Braun., E. Bartscherer, and R. Clasen, "Preparation of Polycrystalline Ceramic Compacts Made of Alumina Powder with a Bimodal Particle Size Distribution for Hot Isostatic Pressing," *Ceramic Engineering and Science Proceedings*, **24** [3] 81-86 (2003).

[22] G. Ferrari, G., "The 'Hows' and 'Whys' of Armour Penetration," *MILTECH*, 81-96 (1988).

[23] R. R. Rigdway, "Boron Carbide. A New Crystalline Abrasive and Wear-Ressisting Product", *Trans. Am. fig:nanosolidfeedElectrochem. Soc.*, **66**, 117-33,(1934).

[24] K. A. Schwetz, "Boron Carbide, Boron Nitride, and Metal Boride," *Ullmann's Encyclopedia of Industrial Chemistry, Sixth Editions*, Wiley-VCH Verlag GmpH, (1999)

[25] T. L. Aselage, and R. G. Tissot, "Latt Const of Boron Carbide," *J. Am. Ceram. Soc.*, **75** [8] 2207-12 (1992).

[26] G. H. Kwei and B. Morosin, "Structures of the Boron-Rich Boron Carbides from Neutron Powder Diffraction: Implications for the Nature of the Inter-Icosahedral Chains," *J. Phys. Chem.*, **100** 8031-8039 (1996).

[27] C. Wood, D. Emin, and P. E. Gray, "Thermal Conduct. of Boron Carbides," *Phys. Rev. B*, **31** [10] 6811-14 (1985).

[28] B. Champagne and R. Angers, "Mechanical Properties of Hot-Pressed B-B_4C Materials," *J. Am. Ceram. Soc.*, **62** [3-4] 149-153 (1979).

[29] P. Rentzepis, D. White and P. N. Walsh, "Heat of Formation of $B_2O_{2(g)}$," *J. Phys. Chem.*, **64**, 1784 (1960).

[30] K. Niihara, A. Nakahira, and T. Hirai, "The Effect of Stoichiometry on Mechanical Properties of Boron Carbide," *J. Am. Ceram. Soc.*, **67** C13-C14 (1984).

[31] F. P. Knudsen, "Dependence of Mechanical Strength of Brittle Polycrystalline Specimens on Porosity and Grain Size, "*J. Am. Ceram. Soc.*, **42** 876-87 (1959).

[32] K. A. Schwetz and W. Grellner, "The Influence of Carbon on the Microstructure and Mechanical Properties of Sintered Boron Carbide," *J. Less Common Metals*, **82** 37-47 (1983).

[33] R. Angers and M. Beauvy, "Hot Pressing of Boron Carbide," *Ceram. Int.*, **10** [2] 49-55 (1984).

[34] T. Vasilos and S. K. Dutta, "Low Temperature Hot Pressing of Boron Carbide and its Properties," *Am. Ceram. Soc. Bull.*, **53** [5] 453-54 (1974).

[35] G. A. Gogotsi, Y. L. Groushevsky, O. D. Dashevskaya, Y. G Gogotsi, and V. A. Lavrenko, "Complex Investigation of Hot Pressed Boron Carbide," *J. Less-Common Met.*, **117** 225-30 (1986).

[36] G. A. Gogotsi, Y. G. Gogotsi, and D. Y. Ostrovoj, "Mechanical Behavior of Hot Pressed Boron Carbide in Various Atmosphere," *J. Mater. Sci. Lett.*, **7**, 814-16 (1988).

[37] M. A. Kuzenkova, P. S. Kislyi, B. L. Grabchuk, and N. I. Bodnaruk, "The Structure and Properties of Sintered Boron Carbide," *J. Less-Common Met.*, **67**, 217-23 (1979).

[38] V. Skorokhod, Jr., M. D. Vlajic, and V. D. Krstic, "Mechanical Properties of Pressureless Sintered Boron Carbide Containing TiB_2 Phase," *J. Mater. Sci. Lett.*, **15** [15] 1337-39 (1996).

[39] H. Suzuki, T. Hasse, and T. Maruhama, "Effect of Carbon on Sintering of Boron Carbide", *Yogyo Kyokai Shi*, **87** 340-33 (1978).

[40] J. W. Henney and W. Grellner, "The Influence of Carbon on the Microstructure and Mechanical Properties of Sintered Boron Carbide," *Brit. Patent. 2,014,193*, (1978).

[41] K. A. Schwetz, W. Grellner, and A. Lipp, "Mechanical Properties of HIP-Treated Sintered Boron Carbide," *Inst. Phys. Conf. Ser. No. 75*, Chapter 5, Adam Hilger Ltd., Bristol, 413-26, 1986.

[42] M. Bougoin and F. Thevenot, "Pressureless Sintering of Boron Carbide with an Addition of Polycarbosilane," *J. Mater. Sci.*, **22**, 109-14 (1987).

[43] F. Thevenot, "Sintering of Boron Carbide and Boron Carbide-Silicon Carbide Two-Phase Materials and Their Properties," *J. Nucl. Mater.*, **152** 154-62 (1988).

[44] S. L. Dole, S. Prochazka, and R. H. Doremus, "Microstructural Coarsening During Sintering of Boron Carbide," *J. Am. Ceram. Soc.*, **72** [6] 958-66 (1989).

[45] S. L. Dole and S. Prochazka, "Densification and Microstructure Development in Boron Carbide," *Ceram. Eng. Sci. Proc.*, **6** [7-8] 1151-160 (1985).

[46] S. Prochazka, S. L. Dole, and C. I. Hejna, "Abnormal Grain Growth and Microcracking in Boron Carbide," *J. Am. Ceram. Soc.*, **68** [9] c235-c236 (1985).

[47] H. Lee and R. F. Speyer, "Pressureless Sintering of Boron Carbide," *J. Am. Ceram. Soc.*, **86** [9] 1468-73 (2003).

[48] R. M. German, *Sintering Theory and Practice*, John Wiley and Sons, New York, 1996.

[49] J. S. Reed, "Principles of Ceramic Processing," 2nd Ed., John Wiley and Sons, New York, 1995.

[50] P. D. Williams and D. D. Hawn, "Aqueous Dispersion an Slip Casting of Boron Carbide Powder: Effect of pH and Oxygen Content," *J. Am. Ceram. Soc.*, **74** [7] 1614-18 (1991).

[51] D. A. Shockey, A. H. Marchand, S. R. Skaggs, G. E. Cort, M. W. Burkett, M. W. and R. Parker, "Failure Phenomenology of Confined Ceramic Targets and Impacting Rods," *Int. J. Impact Engng.*, **9** [3] 263-275 (1990).

[52] J. Radin and W. Goldsmith, "Normal Projectile Penetration and Perforation of Layered Targets," *Int. J. Impact Engng.*, **7** [2] 229-259 (1988).

[53] M. Meyers, *Dynamic Behavior of Materials*, John Wiley and Sons, New York, 1994.

[54] H. Lee and R. F. Speyer "Hardness and Fracture Toughness of Pressureless-sintered B_4C," *J. Am. Ceram. Soc.*, **85** [5] 1291-1293 (2002).

[55] R. C. Weast, Editor, *CRC Handbook of Chemistry and Physics*, 58th Edition, CRC Press, Cleveland, OH, 1977.

[56] J. W. Edington, *Practical Electron Microscopy in Materials Science*, Van Nostrand Reinhold Co., New York, pp. 27-29, 1976.

[57] G. V. Samsonov, Metallphys. Metallkund. SSSR Ural Filial **3-S** 309 (1956), as cited by T. B. Shaffer, "Engineering Properties of Carbides" pp. 804-811, in *Engineered Materials Handbook, Volume 4, Ceramics and Glasses*, S. H. Schneider, Volume Editor, ASM International, Materials Park, OH, 1991.